



3D Modeling of satellite spectral images, radiation budget and energy budget of urban landscapes

Jean-Philippe Gastellu-Etchegorry

► To cite this version:

Jean-Philippe Gastellu-Etchegorry. 3D Modeling of satellite spectral images, radiation budget and energy budget of urban landscapes. Meteorology and Atmospheric Physics, 2008, MAP-0/939, pp.1-21. 10.1007/s00703-008-0344-1 . ird-00405362

HAL Id: ird-00405362

<https://hal.ird.fr/ird-00405362>

Submitted on 20 Jul 2009

HAL is a multi-disciplinary open access archive for the deposit and dissemination of scientific research documents, whether they are published or not. The documents may come from teaching and research institutions in France or abroad, or from public or private research centers.

L'archive ouverte pluridisciplinaire **HAL**, est destinée au dépôt et à la diffusion de documents scientifiques de niveau recherche, publiés ou non, émanant des établissements d'enseignement et de recherche français ou étrangers, des laboratoires publics ou privés.

Centre d'Etudes Spatiales de la Biosphère Paul Sabatier University,
CNES – CNRS, IRD, Toulouse Cedex, France

3D Modeling of satellite spectral images, radiation budget and energy budget of urban landscapes

J. P. Gastellu-Etchegorry

With 15 Figures

Received 16 April 2007; Accepted 27 October 2008
Published online • • 2008 © Springer-Verlag 2008

15 Summary

16 DART EB is a model that is being developed for simulating
17 the 3D (3 dimensional) energy budget of urban and natural
18 scenes, possibly with topography and atmosphere. It simu-
19 lates all non radiative energy mechanisms (heat conduction,
20 turbulent momentum and heat fluxes, water reservoir evo-
21 lution, etc.). It uses DART model (Discrete Anisotropic
22 Radiative Transfer) for simulating radiative mechanisms:
23 3D radiative budget of 3D scenes and their remote sensing
24 images expressed in terms of reflectance or brightness tem-
25 perature values, for any atmosphere, wavelength, sun/view
26 direction, altitude and spatial resolution. It uses an innova-
27 tive multispectral approach (ray tracing, exact kernel, dis-
28 crete ordinate techniques) over the whole optical domain.

29 This paper presents two major and recent improvements of
30 DART for adapting it to urban canopies. (1) Simulation of
31 the geometry and optical characteristics of urban elements
32 (houses, etc.). (2) Modeling of thermal infrared emission by
33 vegetation and urban elements. The new DART> version
34 was used in the context of the CAPITOUL project. For that,
35 districts of the Toulouse urban data base (Autocad format)
36 were translated into DART scenes. This allowed us to
37 simulate visible, near infrared and thermal infrared satellite
38 images of Toulouse districts. Moreover, the 3D radiation
39 budget was used by DARTEB for simulating the time evo-
40 lution of a number of geophysical quantities of various sur-
41 face elements (roads, walls, roofs). Results were successfully

compared with ground measurements of the CAPITOUL 42
project. 43

1. Introduction 44

Modeling the radiative behavior and the energy 45
budget of terrestrial surfaces is relevant for many 46
scientific domains. It is typically the case for 47
studying vegetation functioning with remotely 48
acquired information. For example, the albedo 49
of a canopy with an anisotropic Bidirectional 50
Reflectance Factors (BRF) may be underesti- 51
mated by as much as 45% if it is computed with 52
nadir reflectance only (Kimes and Sellers 1985). 53
Radiative transfer models have the potential for 54
correcting this type of error. However, in order to 55
be efficient tools, models must account for the 56
three dimensional (3D) nature of Earth surfaces. 57
Neglect of the 3D structure of canopies can lead 58
to errors on the 3D radiation budget and remote 59
sensing measurements. For example, it can 60
lead to errors on vegetation BRF and direc- 61
tional brightness temperature (DTDF) distribu- 62
tion functions as large as 50%, depending on 63
instrumental (e.g., view and sun directions) and 64
experimental (e.g., vegetation heterogeneity) con- 65
ditions (Gastellu-Etchegorry et al. 1999). The 66
problem is similar for urban canopies due to their 67

Correspondence: Jean Philippe Gastellu-Etchegorry, Centre
d'Etudes Spatiales de la Biosphère Paul Sabatier University,
CNES – CNRS, IRD 18 avenue Edouard Belin, BPi 2801, 31401
Toulouse Cedex 4, France (E-mail: gastellu@cesbio.cnes.fr)

strong spatial heterogeneity. The application of radiative transfer modeling to urban surfaces is important in the context of the advent of satellite sensors with spatial and spectral resolutions that are more and more adapted to urban characteristics such as building dimensions and temperature spatial variability. It explains the numerous works conducted in the field of remote sensing of urban surfaces (Voogt and Oke 1998; Soux et al. 2004). The use of descriptions with qualitatively based land use data instead of more fundamental surface descriptors is a source of inaccuracy for modeling BRFs and DTDFs (Voogt and Oke 2003).

These remarks stress the usefulness of 3D radiative transfer models. The DART (Discrete Anisotropic Radiative Transfer) model (Gastellu-Etchegorry et al. 1996) was developed in this context for simulating remote sensing images of 3D vegetation canopies in the visible/near infrared (NIR) spectral domain. However, it did not model thermal infrared (TIR) emission and could not operate with urban landscapes. After a brief introduction of DART, this paper presents two major and recent improvements that allow DART to operate on urban landscapes, possibly with vegetation, topography, atmosphere, and atmospheric turbidity within the scene, over the whole optical domain. (1) Simulation of the geometry and optical characteristics of urban elements (houses, etc.). (2) Modeling of TIR emission by vegetation and urban elements. As a result, the present DART model simulates the radiation budget and remote sensing images of natural and urban canopies, for any experimental (sun direction, canopy heterogeneity, topography, more or less turbid atmosphere, etc.) and instrumental (view direction, spatial resolution, etc.) configuration.

The last part of the paper presents results obtained in the context of the CAPITOU project, thanks to the above mentioned improvements. Firstly, visible, NIR and TIR satellite images of Toulouse districts are shown. They were obtained with DART scenes that were directly derived from the Toulouse urban data base (Autocad format). Secondly, an extension of the DART model, called DARTEB (DART energy budget), that is being developed for simulating the 3D energy budget of vegetation and urban canopies is presented. Finally, preliminary results from DARTEB are compared with ground measurements of the CAPITOU project.

2. DART model

DART was originally developed for simulating BRFs, remote sensing images and the spectral radiation budget of 3D natural (e.g., trees, roads, grass, soil, water) landscapes in the visible and short wave infrared domains. Since its first release in 1996, it was successfully tested, in the case of vegetation canopies, against reflectance measurements (Gastellu-Etchegorry et al. 1999) and against a number of 3-D reflectance models (e.g., *Flight* (North 1996), *Sprint* (Thompson and Goel 1998), *Raytran* (Govaerts and Verstraete 1998)), in the context of the RAMI (RADIATION transfer Model Intercomparison) experiment (Pinty et al. 2001, 2004; Widlowski et al. 2007, 2008). Only BRFs could be compared because DART is the only 3-D model that simulates images.

DART was successfully used in many scientific domains: impact of canopy structure on satellite images texture (Pinel and Gastellu-Etchegorry 1998) and reflectance (Gastellu-Etchegorry et al. 1999), 3D distribution of photosynthesis and primary production rates of vegetation canopies (Guillevic and Gastellu-Etchegorry 1999), influence of Norway forest spruce structure and woody elements on LAI retrieval (Malenovsky et al. 2005) and canopy reflectance (Malenovsky et al. 2008), determination of a new hyperspectral index for chlorophyll estimation of forest canopy (Malenovsky et al. 2006), etc.

DART simulates radiative transfer in heterogeneous 3-D landscapes with the exact kernel and discrete ordinate methods. It uses an iterative approach: radiation intercepted in iteration “ i ” is scattered in iteration “ $i + 1$ ”. Any landscape is simulated as a rectangular matrix of parallelepipedic cells. Figure 1 illustrates the way urban and natural landscapes are simulated, possibly with topography and atmosphere. The atmosphere is made of cells the size of which increases with altitude. Radiation is restricted to propagate in a finite number of directions (Ω_i) with an angular sector width ($\Delta\Omega_i$) (sr). Any set of N discrete directions can be selected ($\sum_{n=1}^N \Delta\Omega_n = 4\pi$). A radiation that propagates along direction (Ω_i) at a position r is called a source vector $W(r, \Omega_i)$. It has 3 components: total radiation W , radiation unrelated to leaf mesophyll and polarization degree associated to first order scattering.

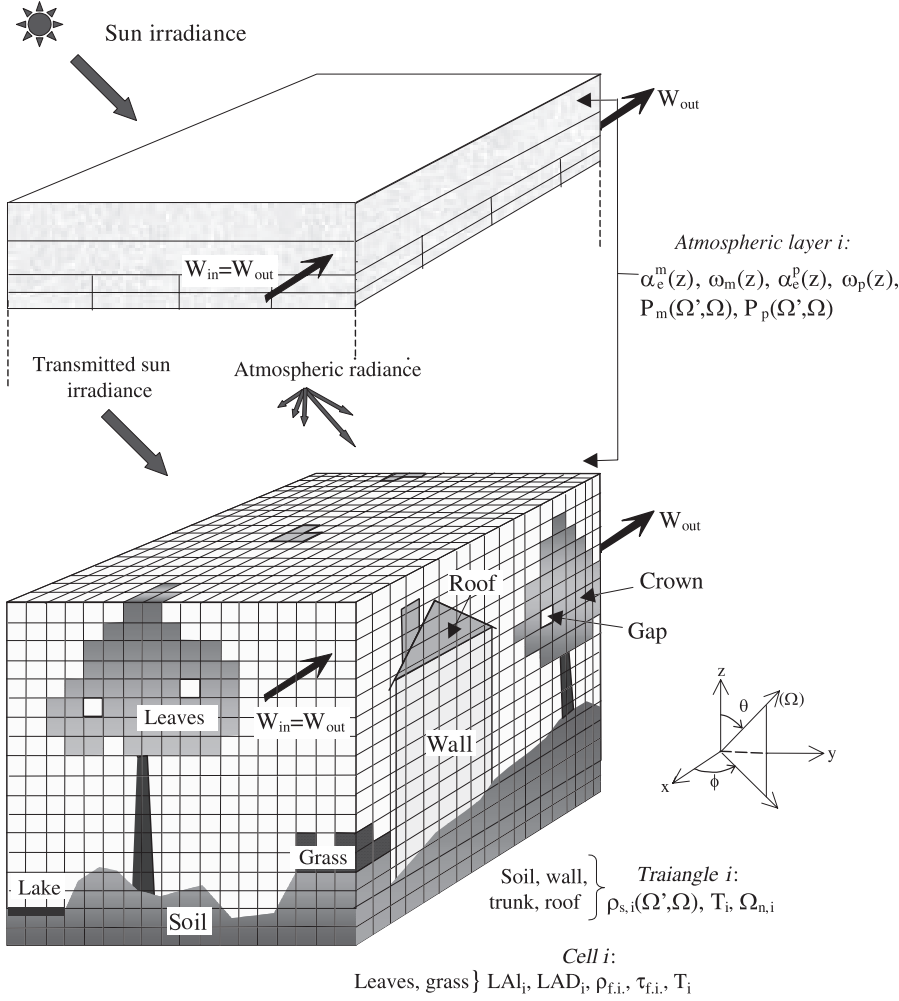


Fig. 1. “Atmosphere + Earth” simulation used as an input to DART model. It shows a mixed “built-up/natural Earth landscape + atmosphere”

1 The number of possible ray paths is finite be-
 2 cause the number of directions is finite and be-
 3 cause within each DART cell, the origin of any
 4 ray is a point P among the N_{sc}^3 points that sample
 5 the cell or the $6 \cdot N_{sf}^2$ points that sample the 6 cell
 6 faces. Thus, there are $(N_{sc}^3 + 6 \cdot N_{sf}^2)$ paths for
 7 each discrete direction, with $N_{sf} = N_{sc}$ for scatter-
 8 ing mechanisms, and $N_{sf} = 2 \cdot N_{sc}$ for emission
 9 mechanisms, usually with $N_{sc} = 7$. In a first step,
 10 DART computes the $(N_{sc}^3 + 6 \cdot N_{sf}^2)$ possible
 11 paths from cell $(0, 0, 0)$. This pre-computation
 12 eliminates unnecessary repetitive computations
 13 during the tracking of source vectors because it
 14 allows a simple calculation of any ray path from
 15 any cell: the coordinates of the i th cell encoun-
 16 tered by a source vector that propagates within
 17 the scene are the coordinates of the cell where it
 18 originates plus the i th coordinates of the pre-
 19 computed ray path that has the same direction.

20 Scene irradiance has 2 components: direct sun
 21 $W(\Omega_s)$ and atmospheric $W_a(\Omega_n)$ source vectors.

$W(\Omega_s)$ propagates along direction (Ω_s) . $W(\Omega_s)$ 22
 and $W_a(\Omega_n)$ are simulated from a fictitious cell 23
 layer on top of the scene (Fig. 1), with values 24
 equal to: 25

$$W(\Omega_s) = E_s(\Omega_s) \cdot |\mu_s| \cdot \Delta x \cdot \Delta y$$

$$W_a(\Omega_n) = L_a(\Omega_n) \cdot |\mu_n| \cdot \Delta x \cdot \Delta y \cdot \Delta \Omega_n$$

where $\Delta x \cdot \Delta y$ is the area of the cell face, $\mu_s =$ 27
 $\cos \theta_s$, $\mu_n = \cos \theta_n$, $E_s(\Omega_s)$ is the solar con- 28
 stant at the top of the scene, and Ω_s denotes 29
 the solar incident direction. $L_a(\Omega_n)$ is the atmo- 30
 spheric radiance along direction (Ω_n) , with 31
 $n \in [1 N']$, where N' is the number of downward 32
 discrete directions. It is null at the top of the 33
 atmosphere. 34

35 Generally speaking, two types of radiation in- 36
 teraction take place. (1) Volume interaction with- 37
 in turbid cells the juxtaposition of which is used 38
 to simulate vegetation elements. (2) Surface in- 39
 teraction on triangles the juxtaposition of which 40
 is used to simulate urban surfaces and topogra-

phy. Radiation interaction within turbid cells is described in Gastellu-Etchegorry et al. (2004). Within cell first order scattering is exactly computed. As expected, simplifying hypotheses are used for simulating multiple scattering. It is now computed with a much faster approach than the initial “harmonic expansion approach: it is computed using the energy intercepted within a finite number of incident angular sectors $\Omega_{\text{sect},k}$ that sample the 4π space of directions ($\sum \Omega_{\text{sect},k} = 4\pi$). The number of sectors can be as large as the number of directions of ray propagation, but a number equal to 6 leads to very accurate results, with relative errors smaller than 10^{-3} (Gastellu-Etchegorry et al. 2004). Another major improvement concerns scattering by turbid cells. Now, scattered radiation starts from a point $M_s(z_{m\uparrow})$ for upward directions (Ω_v) and a point $M_s(z_{m\downarrow})$ for downward directions (Ω_v). The altitudes $z_{m\uparrow}$ and $z_{m\downarrow}$ are those that give exact results for two specific upward $\Omega_{m\uparrow}$ and downward $\Omega_{m\downarrow}$ directions in the case of homogeneous turbid media. Optimal values are $\theta_{m\uparrow} = 20^\circ$ and $\theta_{m\downarrow} = 160^\circ$. These points are computed for each cell face f ($f \in [1, 6]$) that intercepts incident rays, and for each angular sector “incident” on the cell face (Martin 2006). This implies that intercepted vector sources $W_{\text{int}}(f, \Omega_{\text{sect},k})$ are stored per cell face f and per incident angular sector $\Omega_{\text{sect},k}$.

Thus:

$$W_{\text{int}}(f, \Omega_{\text{sect},k}) = \sum_{\Omega_s} W_{\text{int}}(f, \Omega_s),$$

with directions (Ω_s) within ($\Omega_{\text{sect},k}$). For the case “direct sun illumination”, there is only 1 sector.

Atmospheric radiative transfer modeling is implemented for any spectral band in the optical domain from the ultraviolet up to the thermal infrared (Dallest 2001; Gascon 2001). It simulates the atmospheric backscattering phenomenon, which avoids the need to couple DART with an atmospheric model. Atmospheric optical properties are characterized by the molecular $P_m(\lambda, \Omega', \Omega)$ and aerosol $P_p(\lambda, \Omega', \Omega)$ phase functions and by a number of profiles (molecular extinction coefficient $\alpha_e^m(\lambda, z)$ and spherical albedo $\omega_m(\lambda, z)$, aerosol extinction coefficient $\alpha_e^p(\lambda, z)$ and spherical albedo $\omega_p(\lambda, z)$). These quantities are specified by the operator or come from a data base ($[0.3 \mu\text{m} - 30 \mu\text{m}]$) pre-computed with the Modtran atmospheric model (Berk et al. 1989), for a few predefined atmospheres. DART atmo-

spheric reflectance, transmittance and brightness temperature are very close to Modtran simulations in the case of lambertian horizontal Earth surfaces (Grau 2008).

Images are simulated in the focal plane of the satellite sensor (Gentine 2002) with the steps:

- Projection of upward source vectors onto an oversampled horizontal grid on top the scene simulation. The cross section of the emitters and scatterers at the origin of the signal is used for improving the geometric accuracy of images, especially for scenes with marked 3D architectures (urban elements, topography).
- Bi-linear interpolation method that projects the horizontal upper grid of the scene onto an over sampled grid in the sensor plane, at any altitude (bottom to top of the atmosphere).
- Signal convolution with sensor spectral characteristics.

DART works with a specifically designed Graphic User Interface (GUI) for imputing parameters that characterize the landscape and the view and illumination conditions.

3. Simulation of urban elements

Urban elements (e.g., roads, wall, roof) are simulated as the juxtaposition of parallelograms and triangles, hereafter called “opaque figures”. Opaque figures are also used for simulating topography. As a result, DART cells can be empty or filled with either turbid media or plane surfaces. Although all opaque figures undergo the same radiative mechanisms, cells that contain opaque figures (Fig. 2) belong to different cell types (e.g., roof and wall cells) for differentiating their radiation budget. This is used also for obtaining realistic scene displays. The type of a cell that contains all or part of an opaque figure is the type of that opaque figure. Figure 2 shows the

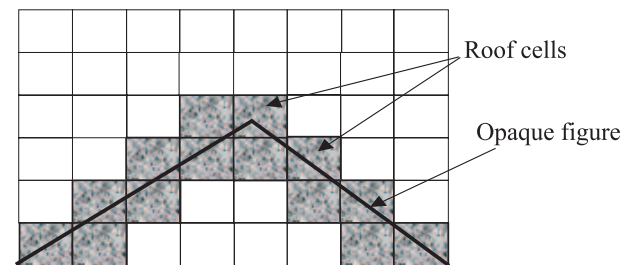


Fig. 2. Cells “Roof” and opaque figures

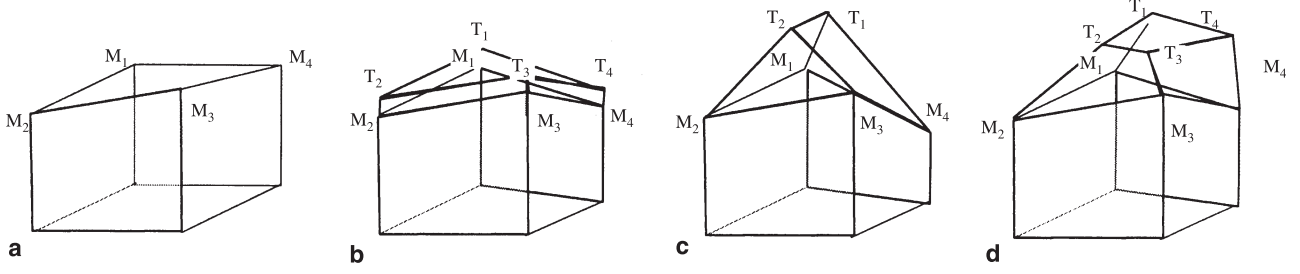


Fig. 3. The 4 pre-defined house types. (a) No roof. (b) Plate. (c) Classic. (d) Complex

intersection of cells with 2 opaque figures that simulate a roof. These cells are called *Roof cells*. Actually, cells can contain or be intersected by several figures. The type of a cell crossed by figures that belong to different urban elements (e.g., roof + wall) is the type of the last simulated urban element.

From the radiative transfer point of view, buildings can have very complex shapes. They are the superimposition of generic volume elements (e.g., tetrahedron, pyramid, column, chimney, etc) defined by any 8 points and 6 faces.

Urban canopy simulation is eased with the pre-definition of four major urban elements:

- *Small wall*: it is defined by its 4 upper corners and its optical properties.
- *House*: it is made of 2 elements (4 walls + 1 roof) simulated by a generic model.

- The 4 walls are defined by their optical properties and their 4 upper corners (x, y, z).
- The roof. Its 4 lower points are the 4 upper corners of the walls, whereas its top is defined by 0 to 4 points, depending on the type of roof (Fig. 3).

- * No roof. The roof is made of 2 triangles that link the top corners of the walls (Fig. 3a).
- * Plate. The roof is a layer defined by a vertical shift (roof depth) from the 4 top wall corners (x, y, z), which defines the 4 points T_1, T_2, T_3 and T_4 of the roof (Fig. 3b).
- * Classic. The roof is defined by the 2 upper points T_1, T_2 of the roof (Fig. 3c).
- * Complex. The roof is defined by the 4 upper points T_1, T_2 of the roof (Fig. 3d).

- *Building*: set of houses with identical optical properties for their walls and roofs.

- *Road*: defined by its width and the coordinates (x, y) of the projection of consecutive points

onto a horizontal plane. The associated segments define the cells called *Route*.

Any radiation scattered $W_{\text{scat}}(\Omega_v)$ by an opaque surface of reflectance $\rho(\Omega_s, \Omega_v)$ is the product of the incident vector source $W_{\text{in}}(\Omega_s)$ by the transfer function $T(\Omega_s, \Omega_v)$, which depends on $\rho(\Omega_s, \Omega_v)$. There are 4 possible types of reflectance:

- *Type 0*: “Lambertian + random spatial variability”.
- *Type 1*: “Lambertian + specular reflectance $\rho_{\text{spec}}(\Omega_s, \Omega_v)$ ”.
- *Type 2*: “Hapke + specular”.
- *Type 3*: Pre-computed functions $T_d(\Omega_s, \Omega_v)$, $T_{\text{spe}}(\Omega_s, \Omega_v)$ and $T_{\text{pol}}(\Omega_s, \Omega_v)$

These 4 types of reflectance and the associated physical laws are presented in the Annex.

Vegetation elements are simulated as the juxtaposition of turbid cells. These cells contain a turbid medium made of infinitesimal planar elements that are characterized by specific optical properties (reflectance, transmittance), a statistical distribution of orientations (LAD: Leaf Angle Distribution) and a surface density (LAI: Leaf Area Index).

4. Ray tracking in presence of opaque figures

Surface scattering and emission mechanisms associated with urban elements are modeled using surface optical properties introduced in the previous chapter. The radiation scattered and/or emitted by opaque figures can be intercepted by other scene elements (i.e., turbid medium or opaque element) within the cell itself and/or other cells (Gastellu-Etchegorry 2007). Approaches adopted for managing ray interception by opaque figures, for determining the origins of rays that are scattered and emitted by opaque figures, and

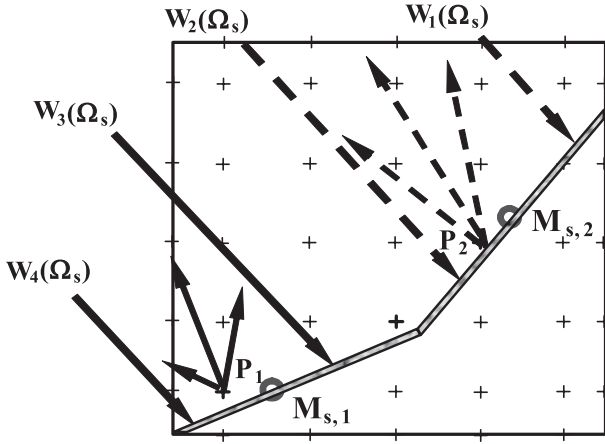


Fig. 4. Interception of 4 rays by 2 figures. W_1 and W_2 are intercepted by Fig. 2. W_3 and W_4 are intercepted by Fig. 1. Resulting effective points of emission are P_2 and P_1

- 1 for tracking rays in presence of opaque figures
- 2 are presented below.

3 4.1 Radiation interception by an opaque figure

4 The within cell interaction “ray – figures (i.e.,
5 triangle/parallelogram)” is modeled in 2 steps:

6 1) Determination if the ray (i.e., $W_1(\Omega_s)$,
7 $W_2(\Omega_s)$, $W_3(\Omega_s)$, $W_4(\Omega_s)$ in Fig. 4) incident
8 on the cell intercepts the plane {point, normal
9 vector} that contains every figure in the cell.

10 2) If there is a point of interception (M), it is
11 checked if this point is both in the cell and
12 in the figure. A test on the co-ordinates of (M)
13 indicates if this point belongs or not to the
14 cell. Two steps allow one to determine if
15 (M) belongs to the figure:

- 16 (i) Change of reference to express the co-ordi-
nates of M in the reference of the figure.
- (ii) These co-ordinates are submitted to N
inequations, associated to N constraints,
 N being the number of edges of the figure.

21 4.2 Origin of radiation scattered/emitted 22 by an opaque figure

23 Rays are scattered and emitted from $(N_{sc}^3 +$
24 $6 \cdot N_{sf}^2)$ predefined points. The determination of
25 these points is carried out in 2 stages:

- 26 1) For each intercepting figure, a barycentric
27 method computes the exact emission point:
28 if a ray intersects a figure in a cell, the new

exact emission point of the figure is the ener-
gy barycentre of this intersection point and
the exact emission point, calculated before
this intersection (e.g., $M_{s,1}$ and $M_{s,2}$ in Fig.
4). This point is always on the figure.

- 2) Determination of the effective point of emis-
sion (e.g., P_1 and P_2 in Fig. 4) among the
 $(N_{sc}^3 + 6 \cdot N_{sf}^2)$ points which sample the cell.
The center (called “sub-center”) of the sub-
cell that contains (M_{si}) is the first guess. It is
determined by thresholding the co-ordinates
of (M_{si}). If it is not acceptable, another point
is searched for. In order to be accepted, a
point P_i must be as close as possible of
(M_{si}) and must verify:

- a) (P_i) is outside the volume bounded by the
emitting figure.
- b) there is no figure between (P_i) and (M_{si}).

The search of the effective point P_i uses a
test on the directions of vectors “sub-center →
figure” and “perpendicular of the figure”. If
these directions are:

- not opposed (i.e., cosine < 0), with no figure
between (M_{si}) and (P_i): (P_i) is accepted.
- opposite: (P_i) is shifted with a sub-grid shift
($\pm \Delta X/N$, $\pm \Delta Y/N$ or $\pm \Delta Z/N$) along the axis
(Ox , Oy or Oz) for which the absolute value of
the component in X , Y or Z of the normal vec-
tor to the figure is largest. ΔX , ΔY , ΔZ are the
cell dimensions.

If no point (P_i) is found both within the cell
and outside the scene element bounded by the
figure, (P_i) is searched in a systematic way
among all possible $(N_{sc}^3 + 6 \cdot N_{sf}^2)$ points (P_i) of
the cell, starting from closer centers. If no point
is found, energy is lost and stored in a variable.
Actually, this energy loss is always negligible.

4.3 Ray tracking from an opaque figure

The interest of effective points of emission (P_i)
is that all possible paths that start from them are
pre-calculated. The actual path of any ray that
comes from a point (P_i) of the cell is pre-cal-
culated as far as the intersection point (Q) of the ray
with the horizontal plane that contains the upper
or bottom face of the cell. Then, the ray follows
the pre-calculated path which originates in the
closer sub-center (E_i) of the horizontal plane.

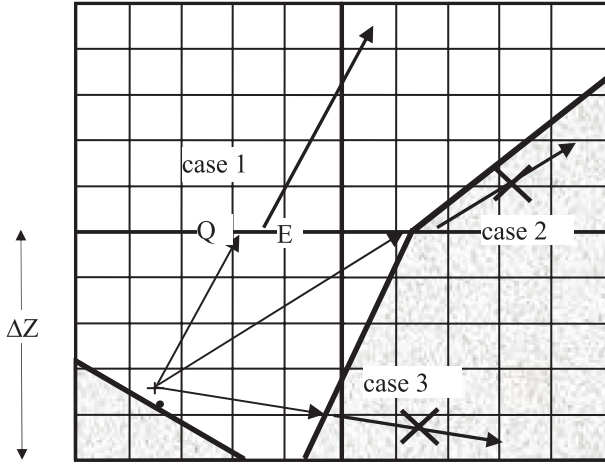


Fig. 5. Illustration of ray tracking in presence of opaque figures

Figure 5 illustrates some cases that occur during ray tracking in presence of opaque figures.

- *Case 1:* Occurrence of a small geometrical shift between the points (Q_i) and (E_i).
- *Case 2:* The ray goes under the figure in the following cell. If the segment ($Q_i E_i$) intersects a figure, the energy of the ray is stored on the first intersected figure.
- *Case 3:* The ray intersects a figure in the cell. If the segment ($Q_i E_i$) intersects a figure of the cell, the energy of the ray is attributed to the closest intercepted figure.

5. Modeling emission mechanisms

TIR modeling was introduced by Boyat (2001) and Guillevic et al. (2003) with methods (i.e.,

discrete ordinate and exact kernel methods, etc.) similar to those used for tracking visible and NIR radiation. Major recent improvements are presented below.

5.1 Thermal emission of leaf turbid cells

Compared to radiative transfer modeling in the short wavelengths, a major specificity of TIR modeling is the emission of turbid leaf cells. Indeed, it is calculated on a cell per cell basis as the integration of the Planck law over a specified spectral band.

• Theoretical approach

Let us consider the radiation $dW_{ij}(\lambda, \Omega_v, T)$ that a cell emits along direction Ω_v , through a surface element S_{ij} of face k of the cell (Fig. 6). The emission comes from the cell volume $V(k, \Omega_v)$.

We have:

$$\begin{aligned}
 dW_{ij}(\lambda, \Omega_v, T) &= L_{B,f}(\lambda, T) \cdot G(\Omega_v) \cdot u_f \cdot \Delta\Omega_v \\
 &\quad \cdot \int_{V(k, \Omega_v)} \exp[-G(\Omega_v) \cdot u_f \cdot \Delta l(dV)] \cdot dV \\
 dW_{ij}(\lambda, \Omega_v, T) &= L_{B,f}(\lambda, T) \cdot \cos(\Psi_{nv}) \\
 &\quad \cdot \Delta\Omega_v \cdot \{1 - \exp[-G(\Omega_v) \cdot u_f \cdot L_{ij}]\} \cdot S_{ij}
 \end{aligned}$$

$L_{B,f}(\lambda, T) = \varepsilon_{f,t} \cdot L_B(\lambda, T)$: radiance of a leaf with temperature T , at wavelength λ .

Ψ_{nv} : angle between direction Ω_v and the normal Ω_n of the face.

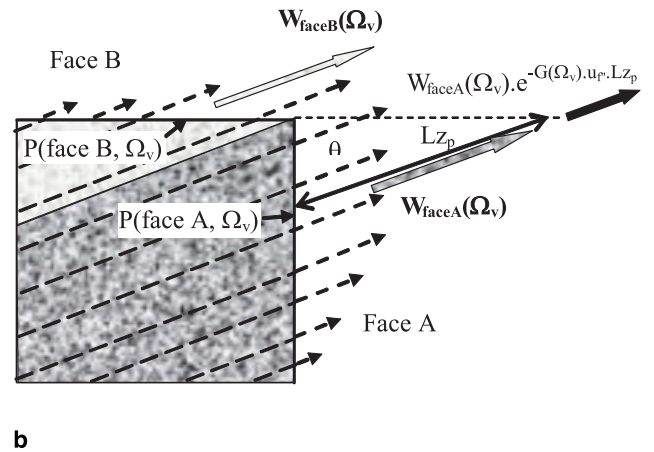
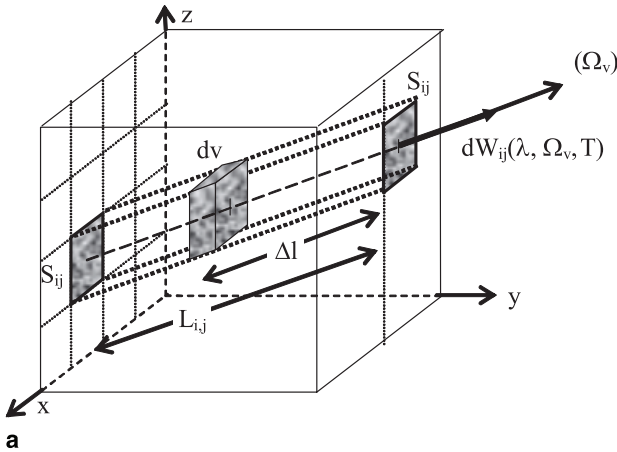


Fig. 6. Computation of the TIR emission of a turbid cell (T, u_f, LAD)

1 Thus, the total emitted energy that crosses face
2 k is:

$$\begin{aligned} W_{1 \text{ face } k}(\Omega_v) &= \sum_{i,j} dW_{ij}(\Omega_v) \\ &= L_{B,f}(\lambda, T) \cdot \cos(\Psi_{nv}) \cdot \Delta\Omega_v \\ &\quad \cdot \sum_{i,j} \{1 - \exp[-G(\Omega_v) \cdot u_f \cdot L_{ij}]\} \cdot S_{ij} \end{aligned}$$

4 If there are \mathcal{T} leaf species $(u_{f,t}, T_t, G_t(\Omega_v))$, with
5 $t \in [1 \mathcal{T}]$, the total emission through face k is:

$$\begin{aligned} W_{1 \text{ face } k}(\Omega_v) &= \frac{\sum_t L_{B,f}(\lambda, T_t) \cdot G_t(\Omega_v) \cdot u_{f,t} \cdot \cos(\Psi_{nv}) \cdot \Delta\Omega_v}{\sum_t G_t(\Omega_v) \cdot u_{f,t}} \\ &\quad \cdot \sum_{i,j} \left\{ 1 - \exp \left[- \sum_t G_t(\Omega_v) \cdot u_{f,t} \cdot L_{ij} \right] \right\} \cdot S_{ij} \end{aligned}$$

7 Source vector $dW_{ij}(\lambda, \Omega_v, T)$ that escapes sur-
8 face S_{ij} along direction (Ω_v) is the sum of the
9 energy emitted by all volume elements dv within
10 volume $S_{ij} \times L_{ij}$. Total energy emitted along (Ω_v)
11 comes from 1 up to 3 cell faces depending on (Ω_v) .

12 • Within cell scattering

13 Part of the TIR emission is intercepted before
14 exiting the cell, which leads to scattering of order
15 1 and larger.

16 Thus, the energy intercepted along the direc-
17 tion (Ω_v) is:

$$\begin{aligned} W_{\text{int}}(\lambda, \Omega_v, T) &= L_{B,f}(\lambda, T) \cdot G(\Omega_v) \cdot u_f \cdot \Delta\Omega_v \\ &\quad \cdot \left\{ V_{\text{cell}} - \frac{\cos \Psi_{nv}}{G(\Omega_v) \cdot u_f} \right. \\ &\quad \cdot \left. \sum_k \sum_{i,j} [1 - e^{-G(\Omega_v) \cdot u_f \cdot L_{ij}}] \cdot S_{ij} \right\} \end{aligned}$$

19 With \mathcal{T} leaf species $(u_{f,t}, T_t, G_t(\Omega_v))$ and $t \in$
20 $[1 \mathcal{T}]$, total energy intercepted along (Ω_v) is:

$$\begin{aligned} W_{\text{int}}(\lambda, \Omega_v, T) &= \sum_t L_{B,f}(\lambda, T_t) \cdot G_t(\Omega_v) \cdot u_{f,t} \cdot \Delta\Omega_v \\ &\quad \cdot \left\{ V_{\text{cell}} - \frac{\cos \Psi_{nv}}{\sum_t G_t(\Omega_v) \cdot u_{f,t}} \right. \\ &\quad \cdot \left. \sum_k \sum_{i,j} [1 - e^{-\sum_t G_t(\Omega_v) \cdot u_{f,t} \cdot L_{ij}}] \cdot S_{ij} \right\} \end{aligned}$$

22 Total interception is:

$$W_{\text{int}}(\lambda, T) = \sum_{v=1}^{N_{\text{dir}}} W_{\text{int}}(\lambda, \Omega_v, T)$$

Scattering radiation that exits the cell is simu- 24
lated as a geometric series: 25

$$\begin{aligned} W_M(\lambda, T) &= W_{\text{int}}(\lambda, T) \cdot \{ \omega_\lambda \cdot \langle T \rangle \\ &\quad + \omega_\lambda \cdot \langle T \rangle \cdot [\omega_\lambda - \omega_\lambda \cdot \langle T \rangle] \\ &\quad + \omega_\lambda \cdot \langle T \rangle \cdot [\omega_\lambda - \omega_\lambda \cdot \langle T \rangle]^2 + \dots \} \\ W_M(\lambda, T) &= \left[\frac{\omega_\lambda \cdot \langle T \rangle}{1 - \omega_\lambda \cdot [1 - \langle T \rangle]} \right] \cdot W_{\text{int}}(\lambda, T) \end{aligned}$$

with $\langle T \rangle$ = mean transmittance on all N_{dir} direc- 27
tions from cell center: 28

$$\langle T \rangle = \frac{1}{4\pi} \cdot \int_{4\pi} e^{-G(\Omega) \cdot u_f \cdot \Delta m(\Omega)} \cdot d\Omega$$

where $\Delta m(\Omega_v)$ = path along (Ω_v) from the cell 30
center to the exit cell face. 31

With \mathcal{T} leaf species 32

$$\begin{aligned} (u_{f,t}, T_t, G_t(\Omega_v)): \omega &= \frac{\sum_t \omega_{f,t} \cdot u_{f,t}}{\sum_t u_{f,t}}, \quad \langle T \rangle = \Pi_t \langle T \rangle_t, \\ G(\Omega_v) \cdot u_f &= \sum_t G_t(\Omega_v) \cdot u_{f,t} \end{aligned}$$

The angular distribution of scattering is: 34

$$W_M(\lambda, \Omega_v, T) = W_M(\lambda, T) \cdot \frac{TG(\Omega_v) \cdot \Delta\Omega_v}{\sum_{v=1}^{N_{\text{dir}}} TG(\Omega_v) \cdot \Delta\Omega_v}$$

with 36

$$\begin{aligned} TG(\Omega_v) &= \sum_{i=1}^{N_{\text{dir}}} T_{\text{diff}}(\Omega_i, \Omega_v) \cdot G(\Omega_i) \cdot \Delta\Omega_i, T_{\text{diff}}(\Omega_i, \Omega_v) \\ &= \int_{\Delta\Omega_v} \frac{\int_{2\pi} \frac{g_f(\Omega_f)}{2\pi} \cdot |\Omega_i \cdot \Omega_f| \cdot f_d(\Omega_f, \Omega_s \rightarrow \Omega_v) \cdot d\Omega_f}{G(\Omega_s)} \\ &\quad \cdot d\Omega_v \end{aligned}$$

With \mathcal{T} leaf species: 38

$$\begin{aligned} TG(\Omega_v) &= \frac{\sum_t TG_t(\Omega_v) \cdot u_{f,t}}{\sum_t u_{f,t}} \Rightarrow W_M(\lambda, \Omega_v, T) \\ &= W_M(\lambda, T) \\ &\quad \cdot \frac{\sum_t TG_t(\Omega_v) \cdot u_{f,t} \cdot \Delta\Omega_v}{\sum_{v=1}^{N_{\text{dir}}} \sum_t TG_t(\Omega_v) \cdot u_{f,t} \cdot \Delta\Omega_v} \end{aligned}$$

The number of faces seen along Ω_v is $K \leq 3$: 40

$$W_M(\lambda, \Omega_v, T) = \sum_{k=1}^K W_{M \text{ face } k}(\lambda, \Omega_v, T, k)$$

- 1 with $W_{M \text{ face } k} \approx$ proportional to leaf area cross
 2 section:

$$S_{\text{eff}}(u_f, \text{LAD}, \Omega_v, k) = \frac{W_{1 \text{ face } k}(\lambda, \Omega_v, T)}{L_B(\lambda, \Omega_v, T)}$$

- 4 Thus:

$$W_{M \text{ face } k}(\lambda, \Omega_v, T) = \frac{W_{1 \text{ face } k}(\lambda, \Omega_v, T)}{\sum_{v=1}^K W_{1 \text{ face } k}(\lambda, \Omega_v, T)} \cdot W_M(\lambda, \Omega_v, T)$$

- 6 Total energy that exits face k along (Ω_v) :

$$\begin{aligned} W_{\text{face } k}(\lambda, \Omega_v, T) &= W_{1 \text{ face } k}(\lambda, \Omega_v, T) \\ &\quad + W_{M \text{ face } k}(\lambda, \Omega_v, T) \\ &\Rightarrow W_{\text{face } k}(\lambda, \Omega_v, T) \\ &= L_B(\lambda, T) \cdot H_f(u_f, \text{LAD}, \Omega_v, k) \end{aligned}$$

- 8 where LAD

$$\begin{aligned} H_f(u_f, \text{LAD}, \Omega_v, k) &= S_{\text{eff}}(u_f, \text{LAD}, \Omega_v, k) \cdot \Delta\Omega_v \\ &\quad \cdot \left[1 + \frac{S_{\text{eff}}(u_f, \text{LAD}, \Omega_v, k)}{\sum_{v=1}^K S_{\text{eff}}(u_f, \text{LAD}, \Omega_v, k)} \right] \\ &\quad \cdot \frac{TG(\Omega_v) \cdot \Delta\Omega_v}{\sum_{v=1}^{N_{\text{dif}}} TG(\Omega_v) \cdot \Delta\Omega_v} \cdot \frac{\omega_\lambda \cdot \langle T \rangle}{1 - \omega_\lambda \cdot [1 - \langle T \rangle]} \\ &\quad \cdot G(\Omega_v) \cdot u_f \cdot \int_{V_{\text{cell}}} (1 - e^{-G(\Omega_v) \cdot u_f \cdot \Delta l(dv)}) \cdot dv \end{aligned}$$

In order to limit computer time, $H_f(u_f, \text{LAD}, \Omega_v, k)$ is pre-computed for:

- all exact $H_f(u_f, \text{LAD}, \Omega_v, k)$ values, if for each leaf species the number of u_f values is ≤ 10 .
- 10 $H_f(u_f, \text{LAD}, \Omega_v, k)$ values, if there is at least one leaf species for which the number of u_f values is > 10 . Pre-computation is performed on 10 equidistant u_f values from $u_{f, \text{min}}$ in to $u_{f, \text{max}}$ for each leaf species. In a 2nd step, the exact $H_f(u_f, \text{LAD}, \Omega_v, k)$ values are computed with a linear interpolation on the u_f values.

The precision of $W(\lambda, \Omega_v, T, k)$ depends on the H_f precision and thus on the discretization level of the sub-faces S_{ij} used to calculate leaf cell emission W_1 and scattering W_M . The estimate of $W(\lambda, \Omega_v, T, k)$ is all the more precise as this discretization is fine; i.e., large number $I \times J$ of sub-faces S_{ij} . Tests conducted with variable values of I and J showed that the pre-defined number $I \times J$ (50×50) lead to errors systematically lower than 0.01 K.

Figure 7 shows DART simulated directional brightness temperature $T_B(\Omega_v)$, as a function of view zenith angle θ_v , for a vegetation turbid medium (LAI=5), with 298 K leaf and soil temperature. It illustrates the impact of (1) the number

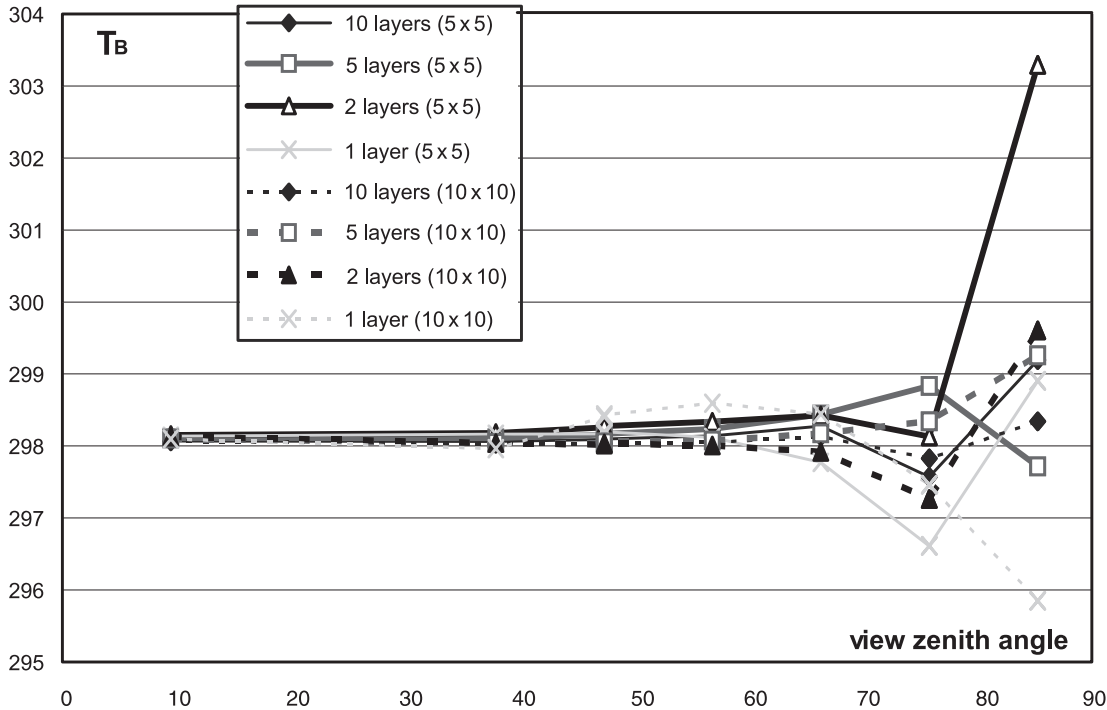


Fig. 7. Precision of $T_{\text{app}}(\Omega_v)$ according to the view zenith angle, the discretization N_{sf} (5×5 or 10×10) and the numbers of layers (1–10). LAI=5. $T_f=298$ K

of $I \times J$ (5×5 and 10×10) sub faces used for computing the emission per cell face, and (2) the number of layers (1, 2, 5 and 10) used to simulate the turbid layer. Brightness temperature should be 298 K for any direction. As expected, errors decrease with the increase of the $I \times J$ value and the number of layers.

• Account of neighbor cells

Usually, the origin of any emitted ray $W_{\text{face } k}$ should not be the center of a cell face. Indeed, the spatial distribution of energy $W_{\text{face } k}(\Omega_v, i, j)$ is not uniform on the exit face k . Moreover, rays $W_{\text{face } k}(\Omega_v, i, j)$ that exit face k have different path lengths in the neighbor cells of the emitting cell, which implies that the transmission of energy $W_{\text{face } k}(\Omega_v, i, j)$, starting from the center of the face k , through several neighbor turbid cells, differs from the sum of energies $W_{\text{face } k}(\Omega_v, i, j)$ transmitted, after exiting face k . Thus, for an upward direction in the Oyz plan (Fig. 6), with cells close to the transmitting cell characterized by a coefficient of projection $G(\Omega_v)$ and a leaf volume density foliar $u_{f''}$, one has:

$$W_{\text{face } k}(\Omega_v) \cdot \exp[-G(\Omega_v) \cdot u_{f''} \cdot \Delta l_{\text{centre}}] \neq < \sum_{i,j} W_{\text{face } k}(\Omega_v, i, j) \cdot \exp[-G(\Omega_v) \cdot u_{f''} \cdot \Delta l_{i,j}]$$

$\Delta l_{i,j}$ = distance from surface dS_{ij} to the horizontal plane of the top face of the emitting cell.

Tracking all individual rays requires much computer resource. Thus, we developed a solution that is both accurate and efficient in terms of computer time, for any type of turbid cell. It determines a point $P(X_P, Y_P, Z_P)$ such that the energy $W_{\text{face } k}(\Omega_v)$ transmitted from P through several neighbor turbid cells is equal to the sum of all individual energies $W_{\text{face } k}(\Omega_v, i, j)$ transmitted. For example, for the right vertical face A (Fig. 6), co-ordinates X_P and Z_P of P verify the two equations:

– coordinate X_P :

$$W_{\text{face } k} \times \exp(-G(\Omega_v) \times u_{f''} \times Lx_P) = \int \int_S (W(x, z, \Omega_v, u_f, \text{LAD}, T, \lambda) \times \exp(-G(\Omega_v) \times u_{f''} \times Lx) \cdot dS)$$

– coordinate Z_P :

$$W_{\text{face } k} \times \exp(-G(\Omega_v) \times u_{f''} \times Lz_P) = \int \int_S (W(x, z, \Omega_v, u_f, \text{LAD}, T, \lambda) \times \exp(-G(\Omega_v) \times u_{f''} \times Lz) \cdot dS)$$

Lz_P : distance along (Ω_v) between a point P of face K and the horizontal plane that contains the upper or lower face of the emitting cell, depending if (Ω_v) is upward or downward.

Lx_P : distance along (Ω_v) between a point P of face K and the vertical plane that contains

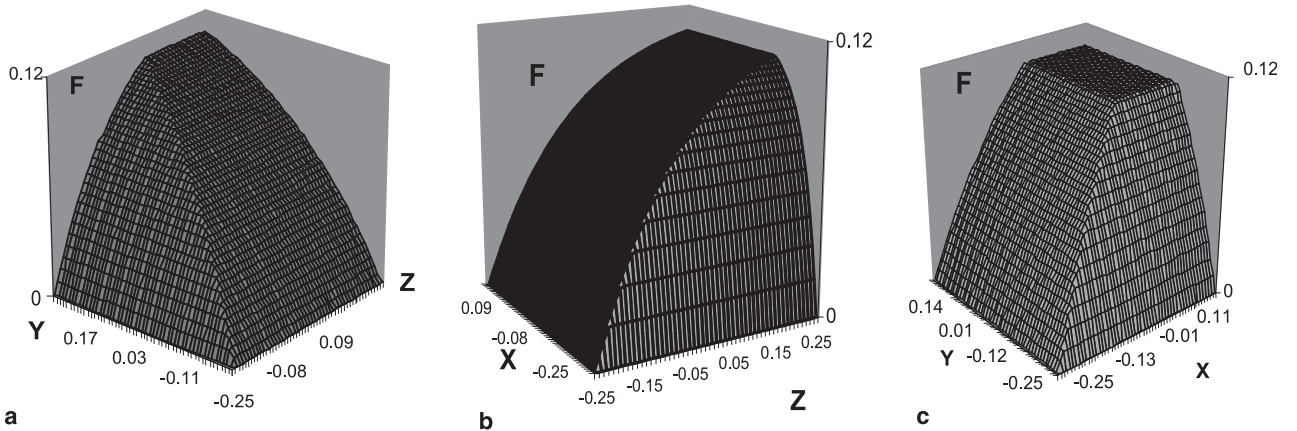


Fig. 8. 3-D relative distributions of the energy emitted by the faces of a turbid cell. (a) Front face ($x = \Delta X$): $F(y, z, \text{LAI}, \text{LAD})$. (b) Right face ($y = \Delta Y$): $F(x, z, \text{LAI}, \text{LAD})$. (c) Top face ($z = \Delta Z$): $F(x, y, \text{LAI}, \text{LAD})$. $\text{LAI} = 5$. $\Delta Y = \Delta Z = 0.5$. LAD spherical. $(\theta_v, \theta_v) = (60, 72)$

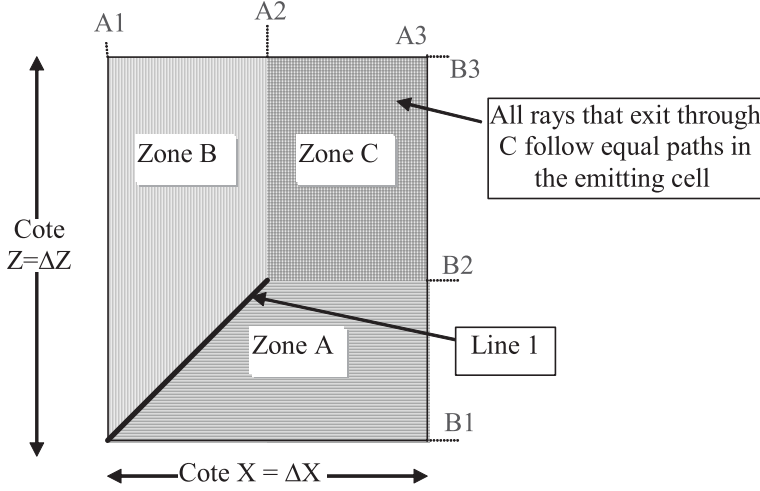


Fig. 9. 3-D schematic representation of distribution F

1 the front or back face of the cell, depending
 2 if (Ω_v) goes forward or backward.
 3 u_f : leaf volume density of the first cell crossed
 4 by the ray from P along (Ω_v) . It can be
 5 null.

6 The energy emitted by a cell along (Ω_v)
 7 through face k is proportional to " $L_B(\lambda, T) \times$
 8 cross section dS_{eff} of face k along (Ω_v) ". Position
 9 of P on face k depends on the relative directional
 10 distribution F of the energy emitted by the cell.
 11 For the cell face in the plane $\{y = \Delta Y\} > 0$, this
 12 distribution is:

$$F(x, z, \theta_v, \varphi_v, u_f, \text{LAD}) = \frac{W(x, z, \theta_v, \varphi_v, u_f, \text{LAD}, T, \lambda)}{L_B(\lambda, T) \times dS_{\text{eff}}}$$

14 Figure 8 shows the relative distribution F
 15 of the emitted energy through the front, right
 16 and top faces of an emitting turbid cell
 17 ($\text{LAI}=5$, $\Delta Y = \Delta Z = 0.5$, spherical LAD),
 18 for direction $(\theta_v, \varphi_v) = (60, 72)$. Face center
 19 $(x, y, z \in [-0.25, 0.25])$ is the origin of co-ordi-
 20 nates. F appears to be the juxtaposition of 3
 21 zones (A, B, C) with generic shapes (Fig. 9)
 22 the limits of which are exponential curves. F
 23 is constant in zone C and has an exponential
 24 surface in zones A and B. These surfaces tend
 25 to be plane surfaces if LAI becomes small.
 26 They are characterized by 6 parameters (A1,
 27 A2, A3, B1, B2, B3) that depend on $(u_f,$
 28 LAD, Ω_v , k) values. These remarks suggest re-
 29 placing the integral expressions of F by analyti-
 30 cal expressions.

The case 'face $y = \Delta Y$ ' is analyzed. $F(x, z,$ 31
 LAI, LAD expressions differ in zones A, B and C: 32

– $M(x, z)$ in zone A ($z < B2$ and $z < a \cdot (x +$ 33
 $\frac{\Delta X}{2}) - \frac{\Delta Z}{2}$): 34

$F_A(x, z, \text{LAI}, \text{LAD})$

$$\omega \cdot \left[1 - \exp \left\{ -\text{sign } e2 \cdot \text{LAI} \cdot \frac{(z - B1)}{|a|} \right\} \right] \\ = \frac{1 - \exp \left\{ -\text{sign } e2 \cdot \text{LAI} \cdot \frac{(B3 - B1)}{|a|} \right\}}{1 - \exp \left\{ -\text{sign } e2 \cdot \text{LAI} \cdot \frac{(B3 - B1)}{|a|} \right\}}$$

– $M(x, z)$ in zone B ($x < A2$ and $z < a \cdot (x +$ 36
 $\frac{\Delta X}{2}) - \frac{\Delta Z}{2}$): 37

$F_B(x, z, \text{LAI}, \text{LAD})$

$$\omega \cdot \left[1 - \exp \left\{ -\text{sign } e1 \cdot \text{LAI} \cdot (x - A1) \right\} \right] \\ = \frac{1 - \exp \left\{ -\text{sign } e1 \cdot \text{LAI} \cdot (A3 - A1) \right\}}{1 - \exp \left\{ -\text{sign } e1 \cdot \text{LAI} \cdot (A3 - A1) \right\}}$$

– $M(x, z)$ in zone C ($x \in [A2, A3]$ and $z \in$ 39
 $[B2, B3]$): $F_C(x, z, \text{LAI}, \text{LAD}) = \omega$ 40

$\text{sign } e1 = \text{sign}(A3 - A1)$

$\text{sign } e2 = \text{sign}(B3 - B1)$

$$a = \frac{B2 - B1}{A2 - A1} \quad u_f = \frac{\text{LAI}}{\Delta Z}$$

$$\omega = \Delta \Omega_v \cdot (1 - \exp(-G \cdot u_f \cdot L))$$

$d\Omega_v$: solid angle of direction Ω_v . 42

L : longer path length of a ray within a cell. 43

a : parameter that allows to ensure the continu- 44
 ity of curves F_A and F_B 45

Function F is not appropriate if the direction 46
 of emission Ω_v is parallel with a face (e.g., 47

1 $\varphi = 90^\circ$). Then, the emission along Ω_v comes
 2 only from 1 or 2 faces (e.g., $\theta = 0$, $\varphi = 0$).

3 Calculation of the 3 co-ordinates of a point ori-
 4 gin P on a cell face, requires to integrate F and to
 5 verify some equations. For example, for the right
 6 face of the cell ($y = \Delta Y$), we must have:

$$W_{\text{face}} \times \exp(-G \cdot u_{f''} \cdot Lx_P) \\ = \int \int_{\text{face}} (F_A + F_B + F_C) \cdot L_B(\lambda, T) \\ \cdot \exp(-G \cdot u_{f''} \cdot Lx) dS_{\text{eff}}$$

$$W_{\text{face}} \times \exp(-G \cdot u_{f''} \cdot Lx_P) \\ = \int \int_{\text{face}} (F_A + F_B + F_C) \cdot L_B(\lambda, T) \\ \cdot \exp(-G \cdot u_{f''} \cdot Lz) dS_{\text{eff}}$$

9 Using:

$$Lx = \frac{(-\text{sign } e(\sin \theta \cdot \cos \varphi)) \cdot \text{Cote } X/2 - x}{\sin \theta \cdot \cos \varphi}$$

$$= \frac{\varepsilon_1 \cdot \text{Cote } X/2 - x}{\sin \theta \cdot \cos \varphi} \quad \text{with}$$

$$\varepsilon_1 = -\text{sign}(\sin \theta \cdot \cos \varphi)$$

$$Lz = \frac{(\text{sign } e(\cos \theta)) \cdot \text{Cote } X/2 - x}{\cos \theta}$$

$$= \frac{\varepsilon_3 \cdot \text{Cote } X/2 - x}{\cos \theta} \quad \text{with } \varepsilon_3 = \text{sign}(\cos \theta)$$

$$Ly = \frac{(-\text{sign } e(\sin \varphi \cdot \sin \theta)) \cdot \text{Cote } Y/2 - y}{\sin \varphi \cdot \cos \theta}$$

$$= \frac{\varepsilon_2 \cdot \text{Cote } Y/2 - y}{\sin \varphi \cdot \sin \theta} \quad \text{with}$$

$$\varepsilon_1 = -\text{sign}(\sin \theta \cdot \cos \varphi)$$

12 co-ordinates of P on the right face of the cell,

13 relative to the center of this cell, are:

$$x_P = \varepsilon_1 - \text{Cote } X/2 + \frac{\cos \varphi \cdot \sin \theta}{G \cdot u_{f''}}$$

$$\cdot \ln \left(\frac{\int \int_{\text{Zone A}} F_A \cdot L \cdot \exp(-G \cdot u_{f''} \cdot Lx) dS_{\text{eff}} + \int \int_{\text{Zone B}} F_B \cdot L \cdot \exp(-G \cdot u_{f''} \cdot Lx) dS_{\text{eff}} + \int \int_{\text{Zone C}} F_C \cdot L \cdot \exp(-G \cdot u_{f''} \cdot Lx) dS_{\text{eff}}}{W_{\text{face}}} \right)$$

$$z_P = \varepsilon_3 \cdot \text{Cote } Z/2 + \frac{\cos \theta}{G \cdot u_{f''}}$$

$$\cdot \ln \left(\frac{\int \int_{\text{Zone A}} F_A \cdot L \cdot \exp(-G \cdot u_{f''} \cdot Lz) dS_{\text{eff}} + \int \int_{\text{Zone B}} F_B \cdot L \cdot \exp(-G \cdot u_{f''} \cdot Lz) dS_{\text{eff}} + \int \int_{\text{Zone C}} F_C \cdot L \cdot \exp(-G \cdot u_{f''} \cdot Lz) dS_{\text{eff}}}{W_{\text{face}}} \right)$$

Expressions of x_P , y_P and z_P are very interesting
 because they are analytical, which makes it pos-
 sible to calculate them with small computation
 times, for any configuration.

If there are \mathcal{T} leaf species, for each direction
 (Ω_v) and each cell face, the point P is the center
 of gravity of all \mathcal{T} points, weighted by the leaf
 volume densities $u_{f,t}$.

5.2 Opaque surfaces

For an opaque surface of direct-hemispheric re-
 flectance $\rho_{\text{dh}}(\lambda, T, \Omega_v) : \alpha_a(\lambda, T, \Omega_v) = 1 - \rho_{\text{dh}}(\lambda, T, \Omega_v)$. Moreover, $\rho_{\text{dh}}(\lambda, T, \Omega_v) = \rho_{\text{hd}}(\lambda, T, \Omega_v)$. Thus, with thermodynamic balance, in the absence of mechanisms of energy exchange other than radiative (Hapke 1993), the emissivity is:

$$\varepsilon_d(\lambda, T, \Omega_v) = \alpha_a(\lambda, T, \Omega_v) = 1 - \rho_{\text{hd}}(\lambda, T, \Omega_v)$$

• Lambertian $\rho_{\text{lamb}} + \text{specular } \rho_{\text{spe,dh}}(\Omega) : \varepsilon_d(\lambda, T, \Omega_v) = 1 - \rho_{\text{lamb}} - \rho_{\text{spe,dh}}(\Omega_v)$

• Hapke $\langle \rho \rangle + \text{specular } \rho_{\text{spe,dh}}(\Omega) : \varepsilon_d(\lambda, T, \Omega_v) = 1 - \langle \rho \rangle - \rho_{\text{spe,dh}}(\Omega_v)$

We consider only the outwards emission, and
 not the inwards emission, by scene elements
 made of opaque figures. Thus, the internal emis-
 sion of houses is not introduced. This choice is
 explained by the fact that DART is mostly dedi-
 cated to the simulation of radiative transfer for
 remote sensing purpose and for the radiative bud-
 get of external surfaces of canopies.

Thus, a surface $(S, \Omega_n, \varepsilon_d)$ emits only in the
 hemisphere that contains its normal (Ω_n) :

$$W_e(\lambda, T, \theta_v) \cong \varepsilon_d \cdot L_B(\lambda, T) \times S \times \cos \psi_{nv} \\ \times \Delta \Omega_v \quad \text{if } \psi_{nv} \leq 90$$

$$W_e(\lambda, T, \theta_v) \cong 0 \quad \text{if } \psi_{nv} \geq 90$$

$$\cos \psi_{nv} = \cos \theta_n \cdot \cos \theta_v + \sin \theta_n \\ \cdot \sin \theta_v \cdot \cos(\psi_{nv})$$

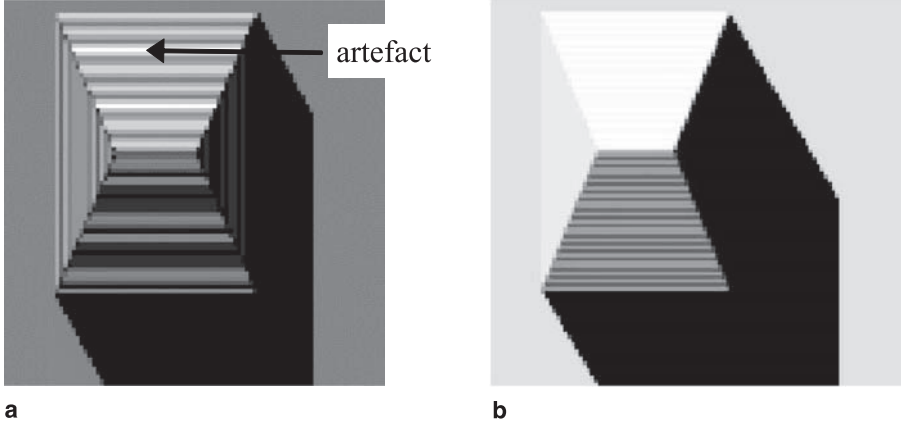


Fig. 10. Computation of T_{figure} , without (a) and with (b) account of the area of figures

1 Once emitted by a cell, a ray $W(\Omega_v)$ is tracked in
2 the 3D scene, where it can be:

- 3 • completely intercepted by an opaque surface,
4 to be scattered in the following iteration, or.
- 5 • partly intercepted by turbid cells or not in-
6 tercepted at all. Part of $W(\Omega_v)$ that reaches a
7 cell $(\Delta X, \Delta Y)$ of scene top layer, increases the
8 energy $W_{\text{c-fict}}(\Omega_v)$ already stored by this cell.

9 After the last iteration, $W_{\text{c-fict}}(\Omega_v)$ is translated
10 into scene brightness temperature $T_B(\Omega_v)$.

$$T_B(\theta_v) = \frac{h \cdot C / \lambda \cdot k}{\ln \left(\frac{2 \cdot h \cdot C^2}{\lambda_o^5 \cdot (W_{\text{c.lop}}(\Omega_v) / \cos(\theta_v) \times \Delta \Omega_v \times \Delta X \times \Delta Y) + 1} \right)}$$

11 In the case of a simulation with $\Delta \lambda \approx 0$, λ_o is
12 the mean wavelength. This choice is not possible
13 if $\Delta \lambda \neq 0$. In that case, the inversion is con-
14 ducted with a reference wavelength that depends
15 on the scene mean temperature T_{mean} (Dallhuin
16 2002). λ_o verifies:

$$L_B(\lambda_o, T_{\text{mean}}) = \frac{1}{\Delta \lambda} \cdot \int_{\lambda_{\min}}^{\lambda_{\max}} L(\lambda, T_{\text{mean}}) \cdot d\lambda$$

$$\neq L \left(\frac{\lambda_{\min} + \lambda_{\max}}{2}, T_{\text{mean}} \right)$$

18 Two approaches can be used to specify the 3D
19 temperature of the scene:

- 20 – 3D matrix of cell temperature values. This ma-
21 trix can be computed by the DARTEB model
22 (see last chapter). In that case, TIR emission
23 of any opaque figure is simulated from the
24 “geometric” barycentre of that figure.

- scene illumination in the visible spectral do-
main. The temperature of any scene element is
proportional to visible scene irradiance and is
within a pre-defined interval that is specific for
each type of scene element: soil, wall, roof,
etc. The limited number of rays that simulate
scene illumination necessarily introduces arti-
facts. These are reduced (1) using a larger
number of illuminating rays per cell of the
scene upper layer (pre defined number is 49),
(2) by accounting the area of each emitting

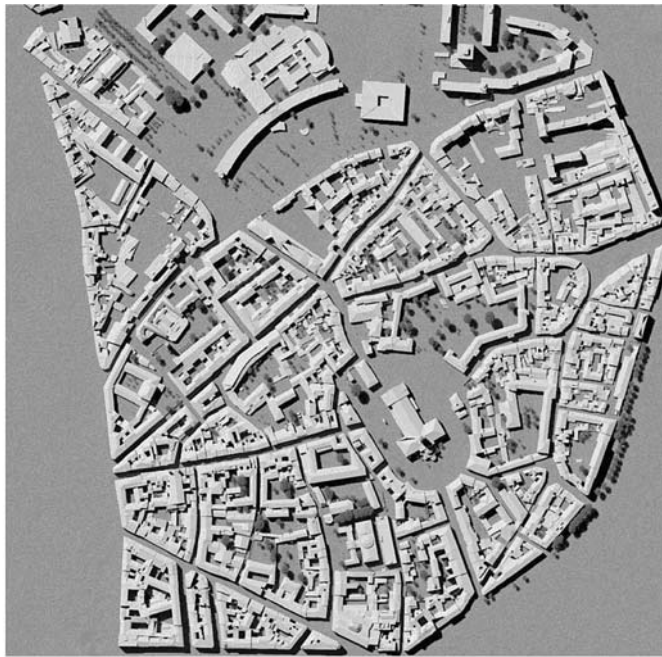
opaque figure (Fig. 10) for calculating its tem-
perature T_{figure} , and (3) by equalizing the tem-
perature of all coplanar figures in the same
cell. TIR emission of opaque figures is simu-
lated from the “energy” barycentre for illu-
minated figures, and from the “geometric”
barycentre for “non illuminated figures”.

6. Application to CAPITOUL project

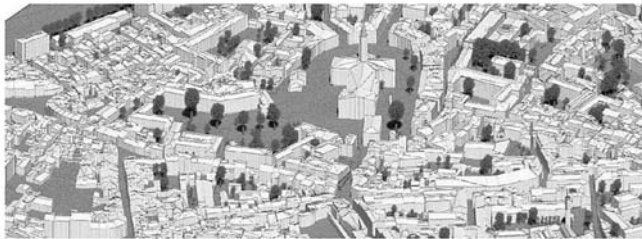
The new DART model was used in the context of
the CAPITOUL experiment that took place over
the city of Toulouse, France, from February 2004
to February 2005. Study of urban energy balance
was one of the objectives. For that, different
types of measurements took place: acquisition
of TIR airborne images, in-situ measurements
of turbulent fluxes, surface energy balance, sur-
face temperatures, etc. (Masson et al. 2007).

1 DART was used for simulating both remote
 2 sensing images in visible, NIR and TIR spectral
 3 bands and the 3D radiative budget. Moreover, the
 4 DARTEB model used this simulated radiative
 5 budget for assessing the time evolution of surface
 6 variables such as wall temperatures and heat sen-
 7 sible fluxes. DARTEB is a model that is being
 8 developed for calculating the 3D (3 dimensional)
 9 energy budget of urban and natural scenes,

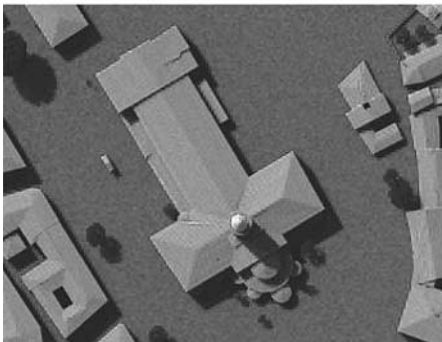
possibly with topography and atmosphere. It ac-
 counts for all energy mechanisms (heat conduc-
 tion, turbulent momentum and heat fluxes, water
 reservoir evolution, vegetation photosynthesis,
 evapotranspiration) that contribute to the energy
 budget. In the case of a urban canopy, it simulates
 non radiative mechanisms with the equations of
 the TEB urban surface scheme (Masson 2000).
 This scheme works with a canyon geometry.



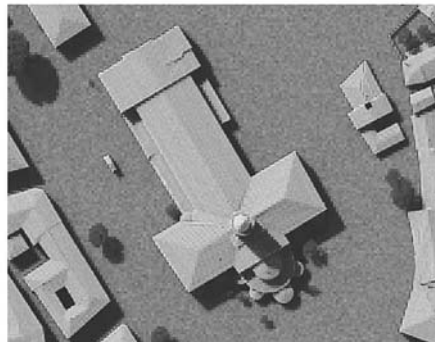
a



b



c



d

Fig. 11. DART simulated nadir (a) and oblique (b) images of St Sernin district. (c) and (d) show the St Sernin basilica (centre (a)) for a sensor below and on top of the atmosphere. Red spectral band

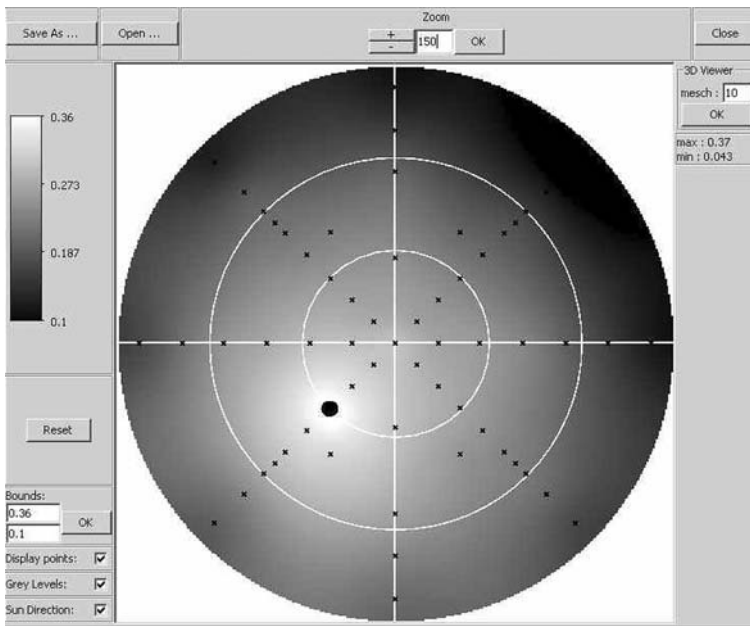


Fig. 12. Example of near infrared BRF of St Sernin district. It is computed by the DART graphic user interface with simulated reflectance values (crosses), for a sun direction shown by a black circle. Distance from the circle centre gives the view zenith angle ([0 90°]) and the anti clockwise angle from the horizontal axis gives the azimuth view angle ([0 360°])

6.1 DART simulated remote sensing images

First, a program was developed for importing the urban database (Autocad format) of the Toulouse town hall as a DART scene. This led to the creation of DART objects (e.g., houses and trees). The fact that urban elements in the data base are not houses or buildings but unrelated individual walls and roofs was a difficulty. The local digital elevation model (DEM) was also imported. Figure 11 shows nadir (a) and oblique (b) color composites of the St Sernin district of Toulouse city. They were created with DART simulations in the blue, green and red spectral bands. Simulations stress that urban reflectance and brightness temperature values display a marked angular heterogeneity. This heterogeneity is illustrated here with the angular distribution of NIR reflectance values of St Sernin district (Fig. 12).

Figure 11c and d display DART remote sensing images of St Sernin basilica, in the center of St Sernin district. They are simulated for a sensor at the bottom of the atmosphere (i.e., BOA image) and for a sensor at the top the atmosphere (TOA). The bluish tone of the TOA image, compared to the BOA image, is due to the fact that atmosphere scatters more in the blue than in the red spectral domain. The realistic aspect of DART images is encouraging. However, the objective of DART is to simulate satellite images

with accurate geometric and radiometric characteristics. This is necessary for studying Earth surfaces from space, using a physical approach such as image inversion (Gastellu-Etchegorry et al. 2003). Although DART was already validated for the visible and NIR spectral domains (Widlowski et al. 2007) and partly validated for the TIR domain (Guillevic et al. 2003), in the future, it should be also validated for TIR radiative transfer in urban canopies with satellite images.

6.2 DARTEB energy budget simulation

DARTEB simulates the energy budget of urban and vegetation canopies. For that, it uses the 3-D DART radiative budget and it models all physical phenomena, other than radiation, that contribute to the energy budget. In the case of urban canopies, turbulent fluxes and conduction are computed with classical boundary-layer laws using equations of the TEB model (Masson 2000). However, conversely to TEB model DARTEB uses a 3-D cell discretization, in addition to the layer discretization of roofs, walls and roads: modeling is conducted on a DART cell per cell basis. As a result, fluxes are computed for each point of the 3-D scene. The transfer coefficients for turbulent heat and moisture fluxes are identical; they differ from the transfer coefficients for momentum fluxes. For DARTEB, the urban can-

1 opy is simulated as the juxtaposition of urban
2 street canyons. Here, we worked with a single
3 urban canyon (Fig. 13), for remaining in the va-

lidity domain of TEB equations (Masson 2000).
 Most major variables used by DARTEB are men-
 tioned in Fig. 13. Each surface type (wall, soil,

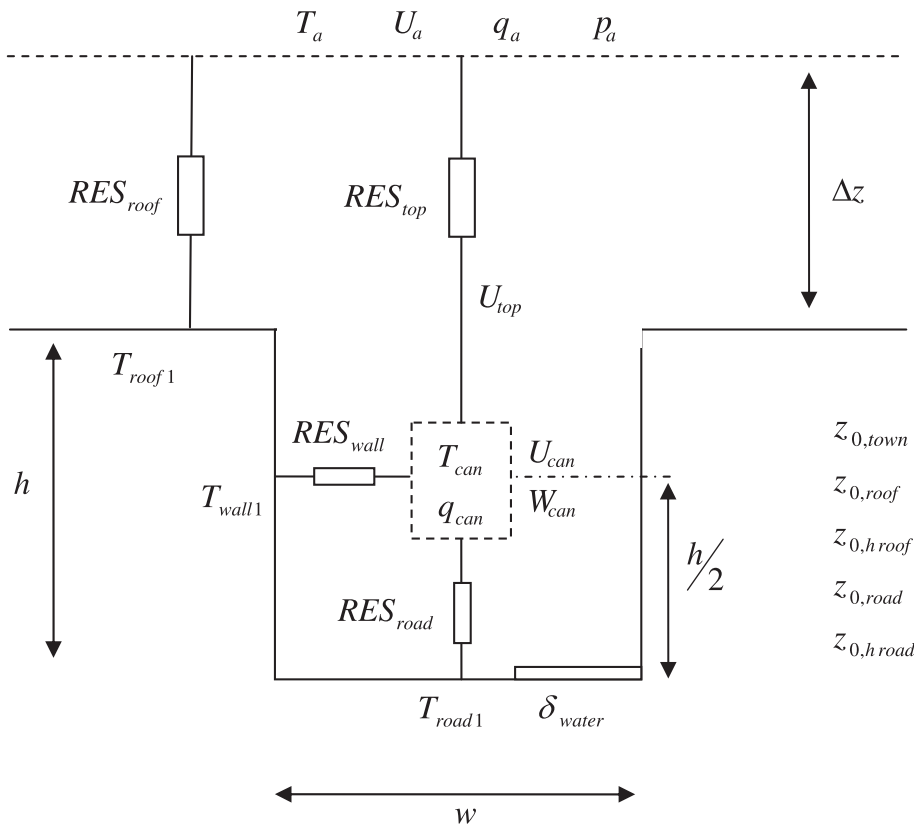


Fig. 13. Simulation of the canyon. Parameters used by DARTEB are listed below. U_a, T_a, q_a, p_a : Wind speed and air temperature/humidity/pressure at 1st atmosphere layer. h, w : Canyon height and width. Δ_z : Height of measurements above the roof, U_{top} : wind speed right above the canyon. $T_{\text{roof}}, T_{\text{wall}}, T_{\text{road}}$: Roof, wall and road temperatures. $\text{RES}_{\text{top}}/\text{RES}_{\text{roof}}$: Aerodynamic resistance between the atmosphere and the canyon/roof, $\text{RES}_{\text{wall}}/\text{RES}_{\text{road}}$: Aerodynamic resistance between the canyon and the wall/road, $U_{\text{can}}/W_{\text{can}}, T_{\text{can}}, q_{\text{can}}$: Canyon horizontal/vertical wind speed and air temperature/humidity, $z_{0,\text{roof}}, z_{0,h \text{ roof}}, z_{0 \text{ road}}, z_{0,h \text{ road}}$: Roof and road dynamic and thermal roughness lengths. $z_{0,\text{town}}$: Town dynamic roughness length. δ_{eau} : Percentage of wet road

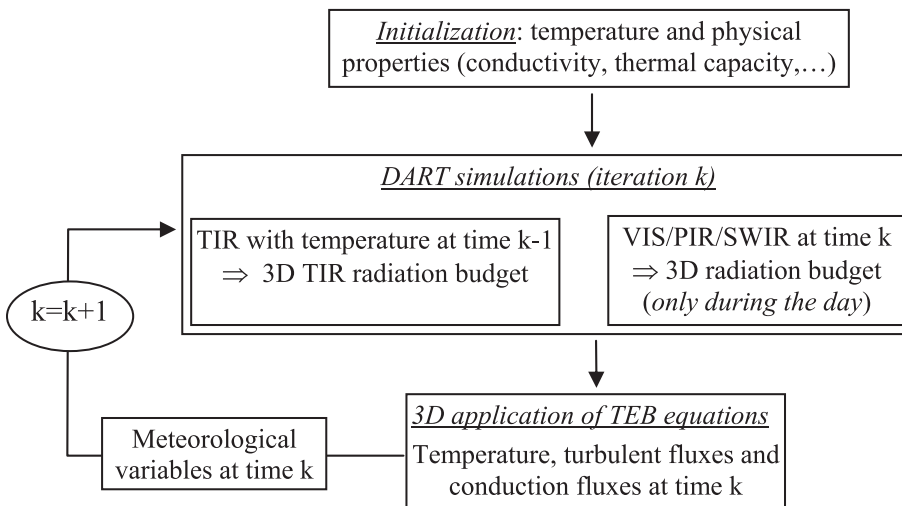


Fig. 14. Diagram of DARTEB model

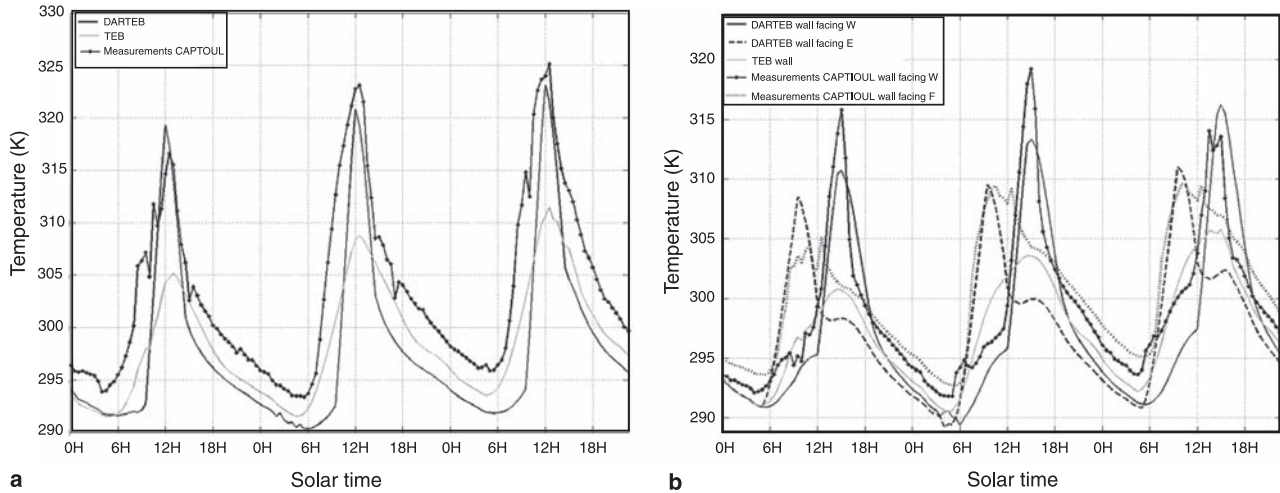


Fig. 15. Comparison of temperature measurements with DARTEB and TEB simulations. July 14–16 2004. **(a)** Road of La Pomme street (Toulouse) with a south East – North West orientation. **(b)** Walls of Alsace Lorraine street (Toulouse) with a South-North orientation. The 2 walls are facing West and East directions, which implies different thermal behaviors

roof) is discretized into several layers for simulating the conduction fluxes to or from the ground and building interiors. The number of layers for road, wall and roof can differ. A minimal number of three layers is advised because temperature gradients can be large and because of the multi-layer structure of the walls and roofs.

DARTEB uses a prognostic approach (Fig. 14) for assessing the 3D radiative budget distribution, and consequently the 3D temperature distribution. Temperature values at time “ $k-1$ ” are used for computing the 3D TIR and energy budgets at time “ k ”, which allows one to compute the 3D temperature distribution at time “ k ”, using the 3D visible and NIR radiation budget at time “ k ” (Fig. 14). DART simulations in the short wave domain are conducted during the day period only.

The validity of DARTEB was tested against TEB simulations and against in situ temperature measurements during the Capitoul campaign (Albinet 2008). DARTEB proved to be coherent with TEB and with measurements. Here, this is illustrated by the comparison of simulated and measured temperatures during 3 days, from July 14 to July 17, 2004, for the Alsace Lorraine street (South-North orientation) and La Pomme street (South East – North West orientation) in Toulouse.

The simulated and measured road temperature curves are very similar (Fig. 15a). As expected, road temperature values increase during the day. There are 3 major differences between DARTEB and TEB simulations. (1) Maximal DARTEB temperatures are larger than maximal TEB temperatures. (2) Maximal DARTEB temperatures occur before midday conversely to maximal TEB temperatures that occur at midday. (3) DARTEB curves are smoother than TEB curves. These differences are mostly explained by the fact that DARTEB takes into account the 3-D nature of the canyon geometry, conversely to TEB.

Indeed, the TEB model works with a mean canyon that corresponds to an azimuthally averaged street direction. Thus, TEB temperatures are mean values, which explains that their time variations are smoothed, with maximal values at midday. Actually, due to the South East – North West orientation of La Pomme street, the maximum road illumination occurs before midday and the maximal road illumination is larger than the mean road illumination for all possible canyon orientations. This is well simulated by DARTEB. Each morning, the measured and DARTEB temperature values display nearly the same sharp increase. However, each afternoon, DARTEB temperature values decrease faster than TEB and the observed temperature values. Several factors can explain the differences be-

tween the DARTEB and observed temperature values. For example, an inaccurate road heat capacity implies an inaccurate conduction flux, and an inaccurate road roughness length tends to imply an inaccurate heat flux, which tends to lead to inaccurate road temperature values. Another possible explanation can come from an inaccurate simulation of the proportions of the 2 components of the canyon illumination: sun and sky illumination. Here, these components are driven by the atmosphere optical depth and sun zenith angle. However, in the absence of measurements, the atmosphere optical depth is assumed to be constant.

The wall (Fig. 15b) DARTEB and measured temperature values tend to be very close, both for the wall facing West, and for the wall facing East. They differ from TEB temperature values because TEB gives a mean value for the 2 walls of the canyon. Account of wall orientation is important because walls with different sun illumination have different temperature values, with larger values during daytime for walls with best sun orientation. As expected, DARTEB maximal temperature values occur in the morning for the wall facing East, and in the afternoon for the wall facing West. This is not the case with TEB maximal temperature values; they occur at midday due to the fact that TEB works with azimuthally averaged canyons. This explains also that TEB temperature values are too small. These examples stress the impact of 3-D architecture on temperature distributions.

7. Conclusion

Some major and recent improvements of DART radiative transfer model are presented in this paper. Thanks to these improvements, the DART model can simulate the radiation budget and remote sensing images of urban and natural landscapes, with atmosphere and topography. Urban landscapes are simulated as the juxtaposition of opaque figures (i.e., triangles and parallelograms). A few basic urban elements are pre-defined for easing the building of urban landscapes: houses with different roofs, low walls, roads, etc. Opaque figures are characterized by specific optical properties: lambertian, specular or Hapke reflectance/emissivity. In order to improve DART radiometric accuracy, the origin of

the path of any scattered and/or emitted ray is either a sub-cell center or a cell sub-face center.

In order to avoid repetitive calculations when simulating radiative transfer, which is costly in terms of computation time, some components of the emission by turbid cells and opaque figures are pre-computed. For example, the intensity that turbid cells emit is pre-computed for each turbid cell type (i.e., ρ_f , τ_f , LAD), for each cell face, for a range of volume density values u_f , and for each direction Ω_v . Moreover, emitted rays start from a point on cell faces, with a location that is analytically computed using pre-computed parameters that depend on the characteristics of the emitting cell and of cells that bound the emitting cell.

DART was used in the context of the Capitoul project (Masson et al. 2007). The objective was to test its potential for simulating remote sensing images and the radiation budget of urban canopies. For that, the Toulouse urban database was imported as a DART scene. Resulting simulated satellite images stressed the potential of DART for urban studies using remote sensing measurements. Moreover, DART simulated 3D radiation budget proved to be a valuable input for modeling the 3D energy budget and heat fluxes with the DARTEB model. Results show that DARTEB simulated temperature values compare very well with in situ measurements, with results even better than TEB model. These better results are surely due to the fact that the DARTEB radiation budget is more accurate than the TEB radiation budget. Moreover, the DARTEB 3-D calculation of fluxes (i.e., on a cell per cell basis) affects also results. Work is being continued for better understanding differences between DARTEB and in situ measurements and TEB simulations on the other hand. An important objective is to determine in which case the account of 3D information, instead of 2D information as in the TEB scheme, is needed for accurate urban studies.

The DART code with the above mentioned improvements was recently professionalized by Magellium (www.magellium.fr) for Linux and Window systems, with the support of French Space Center (CNES). Work is still conducted for obtaining a reference model for remote sensing studies. DART is patented (PCT/FR 02/01181). Paul Sabatier University (France) pro-

vides free licenses for scientific works (www.cesbio.ups-tlse.fr).

Annex

In DART model, there are 4 possible types of reflectance for the opaque surfaces.

- Type 0: “Lambertian + random spatial variability”.

$$\rho(\Omega_s, \Omega_v) = \rho_{\text{lamb}} + \text{standard deviation } \sigma\rho.$$

- Type 1: “Lambertian + specular reflectance $\rho_{\text{spec}}(\Omega_s, \Omega_v)$ ”.

$$\rho(\Omega_s, \Omega_v) = \rho_{\text{lamb}} + \rho_{\text{spec}}(\Omega_s, \Omega_v)$$

DART discretization of directions complicates specular reflectance modeling because there may be no discrete direc-

This allows one to define the direct-hemispheric reflectance factor:

$$\rho_{\text{spe, dh}}(\Omega_s) = \frac{W_{\text{spe}}(\Omega_s)}{W_{\text{int}}(\Omega_s)} = \pi \cdot \left\{ \left[\frac{\text{tg}(\theta_i - \theta_t)}{\text{tg}(\theta_i + \theta_t)} \right]^2 + \left[\frac{\sin(\theta_i - \theta_t)}{\sin(\theta_i + \theta_t)} \right]^2 \right\} \cdot A \cdot \frac{\alpha^4}{64} \cdot \left[1 - \frac{\alpha^2}{72} \right]$$

A surface S illuminated by an isotropic radiance L intercepts $W_{\text{int}}(\Omega_s) = \int L \cdot S \cdot \cos \theta_s \cdot d\Omega_s$. DART discrete directions have small solid angles $\Delta\Omega_i$. Thus:

$$\sum_i \cos \theta_i \cdot \Delta\Omega_i = 2\pi \cdot \sum_i \cos \theta_i \cdot \sin \theta_i \cdot \Delta\theta_i \approx \pi.$$

This allows one to define the hemispheric-hemispheric reflectance factor:

$$\begin{aligned} \rho_{\text{spe, hh}}(\Omega_s) &= \frac{\int W_{\text{spe}}(\Omega_s) \cdot d\Omega_s}{\int W_{\text{int}}(\Omega_s) \cdot d\Omega_s} \approx \frac{\sum_i \pi \cdot \left\{ \left[\frac{\text{tg}(\theta_i - \theta_t)}{\text{tg}(\theta_i + \theta_t)} \right]^2 + \left[\frac{\sin(\theta_i - \theta_t)}{\sin(\theta_i + \theta_t)} \right]^2 \right\} \cdot A \cdot \frac{\alpha^4}{64} \cdot \left[1 - \frac{\alpha^2}{72} \right] L \cdot S \cdot \cos \theta_i \cdot \Delta\Omega_i}{\sum_i L \cdot S \cdot \cos \theta_i \cdot \Delta\Omega_i} \\ &\Rightarrow \rho_{\text{spe, hh}}(\Omega_s) \approx \pi \cdot A \cdot \frac{\alpha^4}{32} \cdot \left[1 - \frac{\alpha^2}{72} \right] \cdot \sum_i \left\{ \left[\frac{\text{tg}(\theta_i - \theta_t)}{\text{tg}(\theta_i + \theta_t)} \right]^2 + \left[\frac{\sin(\theta_i - \theta_t)}{\sin(\theta_i + \theta_t)} \right]^2 \right\} \cdot \cos \theta_i \cdot \sin \theta_i \cdot \Delta\theta_i \end{aligned}$$

tion that coincides with the Fresnel specular direction; *i.e.* a direction that depends on the incident ray direction and on the scatterer orientation.

Specular energy scattered is assumed to occur in a cone of angular width α , with a value $W_{\text{spe}}(\Omega_v^*)$ along (Ω_v^*) that decreases quadratically like “ $\left[\frac{\alpha^2}{4} - \Psi_{\text{vv}^*}^2\right]$ ” from the Fresnel specular direction. Its total value $W_{\text{spe}}(\Omega_s)$ is assumed to be proportional to the intercepted incident radiation $W_{\text{int}}(\Omega_s)$, to the theoretical Fresnel reflectance (*i.e.*, function of the refraction index $n(\lambda)$) and to a weight A .

$$\begin{aligned} W_{\text{spe}}(\Omega_s) &= \int_0^{\alpha/2} \frac{1}{2} \cdot \left\{ \left[\frac{\text{tg}(\theta_i - \theta_t)}{\text{tg}(\theta_i + \theta_t)} \right]^2 + \left[\frac{\sin(\theta_i - \theta_t)}{\sin(\theta_i + \theta_t)} \right]^2 \right\} \\ &\quad \cdot A \cdot \left[\frac{\alpha^2}{4} - \Psi_{\text{vv}^*}^2 \right] \cdot \sin \Psi_{\text{vv}^*} \cdot d\Psi_{\text{vv}^*} \cdot 2\pi \cdot W_{\text{int}}(\Omega_s) \end{aligned}$$

where θ_i and θ_t are the zenith angles of the incident and refracted rays, with $\sin \theta_i = n \cdot \sin \theta_t$

With $\alpha \ll 1$, we have $\sin \Psi_{\text{vv}^*} = \Psi_{\text{vv}^*} - \frac{1}{6} \cdot \Psi_{\text{vv}^*}^3$ for all directions of the specular scattering cone. As a result:

$$\begin{aligned} W_{\text{spe}}(\Omega_s) &= \pi \cdot W_{\text{int}}(\Omega_s) \cdot \left\{ \left[\frac{\text{tg}(\theta_i - \theta_t)}{\text{tg}(\theta_i + \theta_t)} \right]^2 + \left[\frac{\sin(\theta_i - \theta_t)}{\sin(\theta_i + \theta_t)} \right]^2 \right\} \cdot A \cdot \int_0^{\alpha/2} \left[\frac{\alpha^2}{4} - \Psi_{\text{vv}^*}^2 \right] \\ &\quad \cdot \left[\Psi_{\text{vv}^*} - \frac{1}{6} \Psi_{\text{vv}^*}^3 \right] \cdot d\Psi_{\text{vv}^*} \\ W_{\text{spe}}(\Omega_s) &= \pi \cdot W_{\text{int}}(\Omega_s) \cdot \left\{ \left[\frac{\text{tg}(\theta_i - \theta_t)}{\text{tg}(\theta_i + \theta_t)} \right]^2 + \left[\frac{\sin(\theta_i - \theta_t)}{\sin(\theta_i + \theta_t)} \right]^2 \right\} \cdot A \cdot \frac{\alpha^4}{64} \cdot \left[1 - \frac{\alpha^2}{72} \right] \end{aligned}$$

Modeling multiple scattering by specular surfaces uses $\rho_{\text{spe, hh}}(\Omega_s)$. Indeed, for multiple scattering, specular surfaces are assumed to be lambertian with a reflectance coefficient equal to {lambertian reflectance ρ_{lamb} + average specular reflectance $\rho_{\text{spe, hh}}$ }.

It results that $W_{\text{spe}}(\Omega_s)$ is equal to the theoretical specular radiation (Fresnel) weighted by the factor $\pi \cdot A \cdot \frac{\alpha^4}{32} \cdot \left[1 - \frac{\alpha^2}{72} \right]$, usually less than 1. Being reflected in a cone of half angle $\alpha/2$, it must be distributed in all the \mathcal{D} angular sectors $(\Omega_v, \Delta\Omega_v)$ that intersect the specular cone $\Delta\Omega_v = 2\pi \cdot (1 - \cos \frac{\alpha}{2})$. Source vectors $W_{\text{spe}}(\Omega_v, \Delta\Omega_v)$ are computed for any direction $(\Omega_v, \Delta\Omega_v)$ using the approximations and the algorithm presented below.

– Approximations used for ensuring: $\sum_{\mathcal{D}} W_{\text{spe}}(\Omega_v, \Delta\Omega_v) = W_{\text{spe}}(\Omega_s)$. 50

$$W_{\text{spe}}(\Omega_v, \Delta\Omega_v) \approx W_{\text{spe}}(\Omega_s) \cdot \frac{\Delta\Omega_v \cdot \left[\frac{\alpha^2}{4} - \Psi_{\text{vv}^*}^2 \right]}{\sum \Delta\Omega_v \cdot \left[\frac{\alpha^2}{4} - \Psi_{\text{vv}^*}^2 \right]}$$

if $|\Psi_{\text{vv}^*}| < \frac{\alpha}{2}$ and $\Delta\Omega'_v = \Delta\Omega_v \cap \text{specular cone}$

$$W_{\text{spe}}(\Omega_v, \Delta\Omega_v) = 0 \quad \text{if } |\Psi_{\text{vv}^*}| > \frac{\alpha}{2}$$

– Approximations used for avoiding to compute the intersection of solid angles 55

$$\Delta\Omega'_v = \Delta\Omega_v \text{ if } \left\{ \Delta\Omega_v < \Delta\Omega_v^* \quad \text{and} \quad |\Psi_{\text{vv}^*}| < \frac{\alpha}{2} \right\}$$

$$\Delta\Omega'_v = \Delta\Omega_v^* \text{ if } \left\{ \Delta\Omega_v > \Delta\Omega_v^* \quad \text{and} \quad |\Psi_{\text{vv}^*}| < \frac{\alpha}{2} \right\}$$

and $\Delta\Omega'_v = 0$ if $|\Psi_{\text{vv}^*}| > \frac{\alpha}{2}$

1 – Algorithm:

- 2 a) Determination of the angles (θ_v^* , ϕ_v^*) of the specular
 3 direction (Ω_v^*):
 4 Let β the angle between the surface normal Ω_n and the
 incident direction Ω_i . For any Ω_i , $\beta = \theta_v^*$, the vectors
 $\vec{\Omega}_i$, $\vec{\Omega}_v^*$ et Ω_n must be coplanar and the phase angle
 must verify $(\vec{\Omega}_i, \vec{\Omega}_v^*) = 2 \cdot \beta$. With the notation “ $\theta_s =$
 $\pi - \theta_i$, $\phi_s = \phi_i$ ”, $\vec{\Omega}_v^*$ is calculated from: $\vec{\Omega}_v^* + \vec{\Omega}_s =$
 $2 \cos \beta \vec{\Omega}_n$
 10 b) Determination of the \mathcal{D} directions that verify
 11 $|\Psi_{vv^*}| < \frac{\alpha}{2}$.
 12 c) Calculation of $\Delta\Omega_v' \cdot [\frac{\alpha^2}{4} - \Psi_{vv^*}^2]$ for every direction.
- 13 • Type 2: “Hapke + specular”.

$$\rho(\Omega_s, \Omega_v) = \rho_{\text{Hapke}}(\Omega_s, \Omega_v) + \rho_{\text{spec}}(\Omega_s, \Omega_v)$$

15 The component ρ_{Hapke} is calculated with a modeling
 16 that assimilates an opaque figure to a plane medium made
 17 of particles randomly distributed and large compared to
 18 wavelength (Hapke 1993). The phase function $P(g_1, g_2)$
 19 of particles, fitted by a Legendre polynomial, simulates
 20 backscattering and forward scattering (Jacquemoud et al.
 21 1992). Phase angle g_1 is defined as the angle between the
 22 incident sun direction (Ω_s) and the view direction (Ω_v). g_2
 23 is defined as the angle between the specular direction (Ω_v^*)
 24 and (Ω_v):

$$\rho_{\text{Hapke}}(\Omega_s, \Omega_v, \Omega_n) = \frac{\omega}{4} \cdot \frac{1}{\cos(\Psi_{vn}) + |\cos(\Psi_{sn})|} \cdot [[1 + B(g_1)] \cdot P(g_1, g_2) + H(\omega, |\cos(\Psi_{sn})|) \cdot H(\omega, \cos(\Psi_{vn}) - 1)]$$

$$B(g_1) = \frac{B_0}{1 + \frac{1}{h} \cdot \tan\left(\frac{g_1}{2}\right)} \quad H(\omega, x) = \frac{1 + 2 \cdot x}{1 + 2 \cdot \gamma \cdot x}$$

$$\gamma = (1 - \omega)^{0.5}$$

$$P(g_1, g_2) = 1 + b_1 \cdot \cos g_1 + c_1 \cdot \frac{3 \cdot \cos^2(g_1) - 1}{2} + b_2 \cdot \cos(g_2) + c_2 \cdot \frac{3 \cdot \cos^2(g_2) - 1}{2}$$

28 $B(g)$ simulates the hot spot with a height B_0 and a width h .
 29 Model “Hapke + specular” uses 12 parameters:

$$\{\omega, B_0, h, b_1, c_1, g_1, b_2, c_2, g_2\} + \{A, \alpha, n\}$$

31 Multiple scattering is simulated using the assumption
 32 that the surface is lambertian with a reflectance coeffi-
 33 cient calculated by the *phase* module. For the Hapke
 34 model with $b_2 = c_2 = g_2 = 0$, multiple scattering is cal-
 35 culated with:

$$\langle \rho(\Psi_{nv}) \rangle = \frac{1 - (1 - \omega)^{0.5}}{1 + 2 \cdot (1 - \omega)^{0.5} \cdot \cos \Psi_{nv} + \rho_{\text{spe, hd}}(\Omega_v)}$$

- 37 • Type 3: Functions $T_d(\Omega_s, \Omega_v)$, $T_{\text{spe}}(\Omega_s, \Omega_v)$ and $T_{\text{pol}}(\Omega_s,$
 38 $\Omega_v)$ represent the total, specular and polarized reflectance.
 39 They can be used with horizontal surfaces only.

References

- Albinet C (2008) Modélisation 3D des flux et du bilan
 d’énergie des zones urbaines Modélisation des échanges
 d’énergie des milieux urbains. M2 report. Paul Sabatier
 University, Toulouse, France, 57pp
 Berk A, Bernstein LS, Robertson DC (1989) MODTRAN:
 a moderate resolution model for LOWTRAN 7,
 GL-TR-89-0122, Geophys. Lab., Bedford, MA, USA,
 38pp
 Boyat P (2001) Modélisation du transfert radiatif dans le
 domaine thermique des surfaces terrestres. Report. École
 Nationale Supérieure d’Ingénieurs de Constructions
 Aéronautiques, Toulouse, France, 85pp
 Dallest T (2001) Modélisation du transfert radiatif
 atmosphérique dans le domaine de l’infrarouge thermi-
 que. École Nationale Supérieure d’Hydraulique et de
 Mécanique de Grenoble. Report, France, 78pp
 Gascon F (2001) Modélisation Physique d’Images de
 Télédétection Optique. PhD Thesis. Université Paul Saba-
 tier, Toulouse, France
 Gastellu-Etchegorry JP, Demarez V, Pinel V, Zagolski F
 (1996) Modeling radiative transfer in heterogeneous
 3-D vegetation canopies. Remote Sens Environ 58:
 131–56
 Gastellu-Etchegorry JP, Guillevic P, Zagolski F, Demarez
 V, Trichon V, Deering D, Leroy M (1999) Modeling
 BRF and radiation regime of tropical and boreal
 forests – BRF. Remote Sens Environ 68: 281–316
 Gastellu-Etchegorry JP, Gascon F, Estève P (2003) An
 interpolation procedure for generalizing a look-up table
 inversion method. Remote Sens Environ 87: 55–71
 Gastellu-Etchegorry JP, Martin E, Gascon F (2004)
 DART: a 3-D model for simulating satellite images
 and surface radiation budget. Int J Remote Sens 25(1):
 75–96
 Gentine P (2002) Amélioration des images simulées par
 DART. Report. École Nationale Supérieure de l’
 Aéronautique et l’Espace, Toulouse, France, 75pp
 Govaerts Y, Verstraete MM (1998) Raytran. A Monte Carlo
 ray tracing model to compute light scattering in three-
 dimensional heterogeneous media. IEEE Trans Geosci
 Remote Sens 36: 493–505
 Grau E (2008) DART atmosphere radiative transfer model-
 ing, 2008 M2 report, CESBIO
 Guillevic P, Gastellu-Etchegorry JP (1999) Modeling
 BRF and radiation regime of tropical and boreal for-
 ests – PAR regime. Remote Sens Environ 68: 317–40
 Guillevic P, Gastellu-Etchegorry JP, Demarty J, Prévot L
 (2003) Thermal infrared radiative transfer within three-
 dimensional vegetation cover, J Geophys Res Atmos
 ATMOSP 108(D8); DOI: 10.1029/2002JD002247
 Hapke B (1993) Theory of reflectance and emittance spec-
 troscopy. Cambridge University Press, New York
 Jacquemoud S, Baret F, Hanocq JF (1992) Modeling spectral
 and bidirectional soil reflectance. Remote Sens Environ
 41: 123–32
 Kimes DS, Sellers PJ (1985) Inferring hemispherical reflec-
 tance of the Earth’s surface for global energy budgets

- 1 from remotely sensed nadir or directional radiance values.
- 2 Remote Sens Environ 18: 205–23
- 3 Malenovský Z, Martin E, Homolova L, Pokorný R,
- 4 Schaepman ME, Gastellu-Etchegorry J-P, Zurita Milla
- 5 R, Clevers JGPW, Cudlin P (2005) Influence of forest
- 6 canopy structure simulated using the discrete anisotropic
- 7 radiative transfer (DART) model on the retrieval of spruce
- 8 stand LAI. In: 9th International Symposium on Physical
- 9 Measurements and Signatures in Remote Sensing
- 10 (ISPMSRS), Beijing, 17–19 October 2005. Beijing:
- 11 ISPRS WG VII/1, 3pp
- 12 Malenovský Z, Ufer C, Lhotakova Z, Clevers JGPW,
- 13 Schaepman ME, Albrechtova J, Cudlin P (2006) A new
- 14 hyperspectral index for chlorophyll estimation of a forest
- 15 canopy: area under curve normalised to maximal band
- 16 depth between 650–725 nm, EARSeL eProceedings, vol.
- 17 5(2), pp. 161–72
- 18 Malenovský Z, Martin E, Homolová L, Gastellu-Etchegorry
- 19 J-P, Zurita-Milla R, Schaepman ME, Pokorný R, Clevers
- 20 JGPW, Cudlín P (2008) Influence of woody elements of a
- 21 Norway spruce canopy on nadir reflectance simulated by
- 22 the DART model at very high spatial resolution. Remote
- 23 Sens Environ 112: 1–18
- 24 Martin E (2006) DART: Modèle 3D Multispectral et Inver-
- 25 sion d'Images Optiques de Satellite – Application aux
- 26 couverts forestiers. PhD thesis. Paul Sabatier University
- 27 Masson V (2000) A physically-based scheme for the urban
- 28 energy budget in atmospheric models. Bound Layer
- 29 Meteorol 94: 357–97
- 30 Masson V, Gomes L, Pigeon G, Liousse C, Pont V,
- 31 Lagouarde J-P, Voogt JA, Salmond J, Oke TR, Legain
- 32 D, Garrouste O, Lac C, Connan O, Briottet X, Lachérade S
- 33 (2007) The canopy and aerosol particles interaction in
- 34 toulouse urban layer (CAPITOU) experiment. Meteorol
- 35 Atmos Phys, this issue
- 36 North PRJ (1996) Three-dimensional forest light inter-
- 37 action model using a Monte Carlo method. IEEE
- 38 Trans Geosci Remote Sens 34: 946–56
- 39 Pinel V, Gastellu-Etchegorry JP (1998) Sensitivity of tex-
- 40 ture of high resolution images of forest to biophysical
- 41 and acquisition parameters. Remote Sens Environ 65:
- 42 61–85
- 43 Pinty B, Gobron N, Widlowski JL, Gerstl SAW, Verstraete
- 44 MM, Antunes M, Bacour C, Gascon F, Gastellu-
- 45 Etchegorry JP, Jacquemoud S, North P, Qin W, Thompson
- 46 R (2001) Radiation transfer model intercomparaison
- 47 (RAMI) exercise. J Geophys Res 106: D11, 11937–56
- 48 Pinty B, Widlowski J-L, Taberner M, Gobron N, Verstraete
- 49 MM, Disney M, Gascon F, Gastellu J-P, Jiang L, Kuusk A,
- 50 Lewis P, Li X, Ni-Meister W, Nilson T, North P, Qin W,
- 51 Su L, Tang S, Thompson R, Verhoef W, Wang H, Wang J,
- 52 Yan G, Zang H (2004) RAdiation transfer Model Intercom-
- 53 parison (RAMI) exercise: results from the second phase. J
- 54 Geophys Res 109: D06210; DOI: 10.1029/2003JD004252
- 55 Sillon FX, Arvo JR, Westin SH, Greenberg DP (1991) A
- 56 global illumination solution for general reflectance dis-
- 57 tributions. Comput Graph 25: 187–96
- 58 Soux CA, Voogt JA, Oke TR (2004) A model to calculate
- 59 what a remote sensor 'sees' of an urban surface. Bound
- 60 Layer Meteorol 111: 109–32
- 61 Thompson RL, Goel NS (1998) Two models for rapidly
- 62 calculating bidirectional reflectance: Photon spread (Ps)
- 63 model and statistical photon spread (SPS) model. Remote
- 64 Sens Rev 16: 157–207
- 65 Voogt JA, Oke TR (1998) Effects of urban surface geometry
- 66 on remotely sensed surface temperature. Int J Remote
- 67 Sens 19: 895–920
- 68 Voogt JA, Oke TR (2003) Thermal remote sensing of urban
- 69 climates. Remote Sens Environ 86: 370–84
- 70 Widlowski JL, Taberner M, Pinty B, Bruniquel-Pinel V,
- 71 Disney M, Fernandes R, Gastellu-Etchegorry J-P, Gobron
- 72 N, Kuusk A, Laverigne T, Leblanc S, Lewis PE, Martin E,
- 73 Mottus M, North PRJ, Qin W, Robustelli M, Rochdi N,
- 74 Ruiloba R, Soler C, Thompson R, Verhoef W, Verstraete
- 75 MM, Xie D (2007) The third RAdiation transfer Model
- 76 Intercomparison (RAMI) exercise: Documenting progress
- 77 in canopy reflectance models. J Geophys Res 112:
- 78 D09111; DOI: 10.1029/2006JD007821
- 79 Widlowski J-L, Robustelli M, Disney M, Gastellu-
- 80 Etchegorry J-P, Laverigne T, Lewis P, North PRJ, Pinty
- 81 B, Thompson R, Verstraete MM (2008) The RAMI On-
- 82 line Model Checker (ROMC): a web-based benchmarking
- 83 facility for canopy reflectance models. Remote Sens
- 84 Environ 112: 1144–50